Numerical investigation of aerodynamic separation schemes for two-stage-to-orbit-like two-body system

Yue Wang [a,b], Yunpeng Wang [a,b,*], Zonglin Jiang [a,b]

[a] *State Key Laboratory of High Temperature Gas Dynamics, Institute of Mechanics, Chinese Academy of Sciences, 100190 Beijing, China*
[b] *School of Engineering Sciences, University of Chinese Academy of Sciences, 100049 Beijing, China*

A R T I C L E   I N F O

A B S T R A C T

Two-stage-to-orbit (TSTO) hypersonic vehicle is considered one of the most promising next-generation reusable launch vehicle (RLV) systems for its efficiency and reliability, but the safe separation of two-body system determines the success of TSTO missions. Hypersonic flows around a TSTO-like two-body system are studied by CFD (computational fluid dynamics) dynamic simulations at Mach 7. The TSTO model, which consists of two three-dimensional (3-D) wedges as orbiter and booster, is used to investigate the interstage aerodynamic interferences and separation characteristics with different stage separation schemes. This paper analyzes in detail the transverse stage separation (TSS) scheme, where the orbiter moves along the direction normal to the upper surface of the booster. Besides, the longitudinal stage separation (LSS) scheme, in which the orbiter moves rapidly along the flight direction of the booster, is proposed. The numerical results of dynamic simulation show that the complex interstage aerodynamic interference is accompanied by the combined action, including the disturbance of wave/boundary-layer interaction, shock/wake-flow interaction, and a horseshoe vortex (or a "∧" vortex). Moreover, the flow characteristics and the physical mechanism of TSTO separation are clarified by analyzing the changes of flow structure and the topologies of 3-D separation flow. The intensity of the aerodynamic interference increases with increasing angle of incidence (AoI), but decreases with the increase of clearance during TSS. The ideal values of AoI for TSTO TSS are 6° and 8°. For LSS, the orbiter can safely separate from the booster at angle of attack (AoA) = 5° and 10° cases while the collision occurs at AoA = 0° case. The proper AoA value of the safe LSS is 5°. Since the interference load on the stages in LSS is smaller than that in TSS, the LSS is ideal for stage separation of TSTO.

© 2022 Elsevier Masson SAS. All rights reserved.

1. Introduction

Shock/shock and shock/boundary-layer interaction (SSI & SBLI) in two-body systems typically lead to crucial aerodynamic and aerothermal problems for aerospace vehicles at supersonic and hypersonic speeds [1–5]. Two-body systems are often used in various aerospace applications, such as the Two-stage-to-orbit (TSTO) hypersonic vehicles, the next generation of the reusable launch vehicle (RLV) [6,7] for space transport. Besides, TSTO is considered to be the most promising RLV due to its significant advantages, such as small mass, large payload, and efficiency on the propulsion systems [8–13]. Therefore, it has been widely investigated in the past few decades. TSTO consists of an orbiter with reusable rocket engines and a booster with airbreathing turbo/ramjet propulsions

[14,15]. Hence, TSTO stage separation usually occurs in the hypersonic flow regime, leading to the strong SSI and SBLI between the two stages. These interactions can affect the force and moment characteristics and change the subsequent trajectory of the stages. Thus, the safe stage separation determines the success of the TSTO mission, and the evaluation of the stage separation schemes for TSTO is critical. Besides, the deeper understanding of the associated flow physics and TSTO aerodynamic characteristics during stage separation is also instructive for the design and control of the TSTO safety separation.

Currently, little information in the open literature on the effects of aerodynamic separation between TSTO stages at hypersonic speeds is available. Moreover, several studies have focused on TSS aerodynamics, and the interference effects between two stages during separation have been investigated statically and dynamically. Moelyadi et al. [16] investigated the aerodynamic interference pattern and the aerodynamic coefficients of the TSTO system with different Mach numbers and two-stages relative positions. The results suggested that mutual interference was induced

Nomenclature

AoA	angle of attack	°
AoI	angle of incidence	°
F_T	thrust on the orbit	N
h	interstage clearance	m
d	height of stage	m
m	mass	kg
I_{xx}	moment of inertia about X-axis	kg·m²
I_{yy}	moment of inertia about Y-axis	kg·m²
I_{zz}	moment of inertia about Z-axis	kg·m²
ρ	density	kg·m⁻³
l	length of stage	m
w	width of stage	m
g	gravitational acceleration, 9.8 m·s⁻²	
$\boldsymbol{W}$	vectors of conservative variables	
$\boldsymbol{F}_c$	convective fluxes	
$\boldsymbol{F}_v$	viscous fluxes	
u, v, w	velocity components in x, y, and z directions	m·s⁻¹
p	pressure	Pa
E, H	total energy and total enthalpy per unit mass	J·kg⁻¹
$\tau_{i,j}$	component of viscous stress	N·m⁻²
Θ	heat conduction	W·m⁻²
$\boldsymbol{V}_r$	contravariant velocity vector relative to the motion of the grid	m·s⁻¹
$\boldsymbol{V}_g$	contravariant velocity vector at the surface of the control volume	m·s⁻¹
T	temperature	K
dt	physical time step	s

Ma	Mach number	
Re	Reynolds number	
V_x, V_y, V_z	velocity components of body	m·s⁻¹
$\omega_x, \omega_y, \omega_z$	angular velocity components of body	s⁻¹
F_x, F_y, F_z	force components exerted on body	N
M_x, M_y, M_z	moment components exerted on body	N·m
y^+	non-dimensional wall spacing	
C_p	pressure coefficient	
C_f	skin fraction coefficient	
x	coordinate in the X direction	m
$\nabla\rho$	density gradient	kg·m⁻⁴
ΔC_L	difference of lift coefficient	
C_L	lift coefficient	
C_D	drag coefficient	
C_M	pitching moment coefficient	
Δx	X-displacement of the orbiter	m
Δy	Y-displacement of the orbiter	m
t	time	ms
h_g	minimum gap between two stages	m
ΔC_M	difference of pitching moment coefficient	

Subscripts

CG	center of gravity
∞	freestream conditions
o	orbiter conditions
b	booster conditions
iso	isolated conditions

by the incident and reflected shock waves and expansion waves. An experimental study of the TSTO system with various clearances between stages at Mach 8.1 was performed by Ozawa et al. [17,18]. The TSTO system was simplified into a Hemisphere-Cylinder/Flat plate two-body configuration. The result showed that the clearance between stages plays a significant role in the flowfield and heat-flux on the wall. Kitamura et al. [19,20] studied the effects of the aerodynamic interference between a Hemisphere-Cylinder and a Delta Wing at Mach 8.1. They revealed that the increment of heat-flux at the nose varies with clearance. Bordelon et al. [21] conducted stage separation tests for the TSTO model and suggested that the TSTO vehicle is statically unstable in several separation positions because of strong shock interactions. In short, most studies have focused on stage separation aerodynamics through numerical simulations and experiments on static two-body systems. However, investigating the dynamic separation behavior is essential because the relative motions among the two stages are affected by the unsteady aerodynamic interference during stage separation.

Due to the complexity of the dynamic separation for the two-body system, computational fluid dynamics (CFD) is regarded as an economical and efficient alternative compared with the wind tunnel test. Thus, there has been considerable research on the dynamic separation of the two-body system using CFD. Brenner [22] performed a dynamic inviscid simulation of multiple bodies in relative motion, and the results showed a slow transient aerodynamic interference during separation between stages and the feasibility of dynamic simulations. Cvrlje et al. [23] simulated the unsteady flow around an idealized TSTO model during stage separation at Mach 6.8. They investigated the aerodynamic characteristic of orbiters that oscillated at given frequencies in yaw and roll directions at a certain clearance. The results indicated that unsteadiness could not be neglected in the stability and control evaluations for lateral motion (i.e., Transverse stage separation (TSS) in the present study). Liu et al. [11] numerically investigated the aero-

dynamic interference and separation process of TSTO vehicles with the turbo-based combined cycle engines. The results showed that the method to change flap pre-deflection has limited effect on improving the safety of stage separation, and a safe separation model can be achieved at the $-2°$ angle of attack (AoA). The separation of a bomb and fuel tank from an aircraft was simulated using the 6 - Degree of Freedom (6-DOF) procedure by Olejnik et al. [24], and the CFD results were in good agreement with the wind tunnel test data. Song et al. [25] conducted a free-flight test of multi-body stage separation at Mach 1.5 and evaluated the effects of the initial launch AoA and separation velocity on stage separation compatibility. Xue et al. [26] described a design method using a similarity law for aircraft load separation test, considering the effects of initial separation velocity on the motion similarity. The results showed that the new similarity law greatly improved the test accuracy. Wang et al. [27,28] analyzed the influence of separation distance on the capsule-shaped abort system at Mach 3 and found that the unsteady flow oscillation was a potential risk during the separation of the capsule and rocket.

Most researchers have focused on studying the aerodynamic interference in terms of TSS for two-body systems, and some studies have examined the safe stage separation for the tandem configuration of multi-body systems (e.g., multi-stage rocket) [29]. However, alternative separation schemes, such as longitudinal stage separation (LSS) for parallel TSTO configuration, have not been considered. Moreover, the detailed flow mechanism involving the dynamic aerodynamic interference, especially in three-dimensional (3-D) separation flow, is not sufficiently clear because of the complexity during TSTO stage separation. Thus, the LSS scheme for parallel TSTO configuration is proposed, and CFD dynamic simulations of the TSS and LSS schemes for TSTO systems are reported in this paper. The TSTO system is composed of two wedges that act as an orbiter and a booster. This study aims to reveal the detailed physical mechanism of dynamic 3-D interactions and separation

Fig. 1. The real view example of the TSTO vehicle of the Sanger concept [30].

flow between stages for two aerodynamic separation schemes of TSTO and to analyze the aerodynamic interference influence on the characteristics of vehicle force and moment. Finally, the influence of the angle of incidence (AoI) and AoA on the TSS and LSS for the current TSTO model are studied, respectively. Also, the performance of each separation scheme is compared and discussed.

2. TSTO-like two-body models and two stage separation schemes

Fig. 1 presents a real view example of the TSTO vehicle of the Sanger concept [30]. The model of the TSTO-like two-body system considered in this study is simplified from the Sanger TSTO configuration, with a reduction in scale, and its schematic illustration is presented in Fig. 2 (a). The wedge model is used for its universality in hypersonic fundamental research and efficiency of computations. Fig. 2 (b) presents the schematic of the TSTO aerodynamic separation schemes in the current study. The separation schemes proposed here include TSS and LSS, based on the classification of the traditional space separation criterion [31]. In Fig. 2, the AoA is defined as the angle between the upper wall of the booster and the freestream velocity. The AoI is defined as the orbiter incidence angle relative to the booster, i.e., the angle between the lower wall of the orbiter and the upper wall of the booster, is varied by manual adjustment. The TSS refers to the orbiter release freely with appropriate AoI and AoA = 0 during stage separation, while the LSS means the orbiter accelerated on the back of the booster with the rocket-power thrust (F_T) at a positive value of AoA. Moreover, the initial clearance between stages for both separation schemes is $h/d_o = 0.26$ for the convenience of comparing the two separation schemes and conducting numerical simulations, despite the ideal situation of LSS is no or minimal clearance between the two stages. For the computation of LSS, the simulation is divided into two stages: First, the orbiter is accelerated by the thrust in the constrained vertical and pitching motion. Second, the orbiter is freely separated from the booster in 6-DOF motion when the orbiter nose coincides with the booster nose. Besides, the dynamic simulation cases of TSTO stage separation in this study are shown in Table 1. In all cases, the booster is assumed to be fixed, and the orbiter rotates around the center of gravity (CG) under the action of aerodynamic moments. The mass of the orbiter is $m_o/\rho_\infty \cdot l_o^3 = 100$, and the moment of inertia are $I_{xx}/\rho_\infty \cdot l_o^5 = 60$, $I_{yy}/\rho_\infty \cdot l_o^5 = 125$, and $I_{zz}/\rho_\infty \cdot l_o^5 = 100$, respectively. Herein, ρ_∞ refers to the density of freestream. Besides, the mass of the orbiter and the moment of inertia are evaluated by the CAE software with the assumption of the material of the model to be aluminum alloy.

3. Numerical simulation

3.1. Governing equations and numerical methods

The unsteady compressible Navier-Stokes (N-S) equations in integration form are used for the dynamic simulations of two-body separation:

$$\frac{\partial}{\partial t} \iiint_\Omega \boldsymbol{W} d\Omega + \oiint_{\partial\Omega} (\boldsymbol{F}_c - \boldsymbol{F}_v) d\boldsymbol{S} = 0 \qquad (1)$$

Table 1
Specifications for the dynamic stage separation cases in this study.

Case	Separation scheme	AoA [°]	AoI [°]	Remark
1			4	
2			6	
3	TSS	0	8	Free-release
4			10	
5			12	
6		0		
7	LSS	5	0	$F_T/m_o g = 480$
8		10		

where $\boldsymbol{W}$, $\boldsymbol{F}_c$, and $\boldsymbol{F}_v$ are the vectors of conservative variables, convective fluxes, and viscous fluxes, respectively, which are expressed as:

$$\boldsymbol{W} = \begin{pmatrix} \rho \\ \rho u \\ \rho v \\ \rho w \\ \rho E \end{pmatrix}, \qquad \boldsymbol{F}_c = \begin{pmatrix} \rho V_r \\ \rho u V_r + n_x p \\ \rho v V_r + n_y p \\ \rho w V_r + n_z p \\ \rho H V_r + V_g p \end{pmatrix},$$

$$\boldsymbol{F}_v = \begin{pmatrix} 0 \\ n_x \tau_{xx} + n_y \tau_{xy} + n_z \tau_{xz} \\ n_x \tau_{yx} + n_y \tau_{yy} + n_z \tau_{yz} \\ n_x \tau_{zx} + n_y \tau_{zy} + n_z \tau_{zz} \\ n_x \Theta_x + n_y \Theta_y + n_z \Theta_z \end{pmatrix}, \qquad (2)$$

where ρ represents the density, u, v, and w represent the velocity components in x, y, and z directions, respectively, p represents the pressure, E and H represent the total energy and total enthalpy per unit mass, respectively, τ_{ij} represents the component of viscous stress, Θ_x, Θ_y, and Θ_z express the heat conduction, n_x, n_y, and n_z represent the unit normal vector of the control body surface, and V_r represents the normal velocity of the control volume surface relative to the grid motion.

$$V_r = V - V_g = (u - u_g) n_x + (v - v_g) n_y + (w - w_g) n_z \qquad (3)$$

Where $V_g = u_g n_x + v_g n_y + w_g n_z$ is the normal velocity of the surface of the control volume. Additionally, to close the system of equations, it is necessary to introduce the ideal gas equation of state:

$$p = \rho R T. \qquad (4)$$

In the current study, the N-S equations are solved by the finite volume method. The Harten-Lax-van Leer contact (HLLC) approximate Riemann scheme [32] with the minmod limiter [33] is used to compute the second-order convective flux $\boldsymbol{F}_c$. The viscous flux $\boldsymbol{F}_v$ is computed by a simple second-order average of all vertex polynomials. Moreover, the coefficient of viscosity is evaluated by Sutherland's law [34]. Time advancement is performed by implicit backward Euler integration with multi-grid acceleration and dual time-stepping methods [35]. In order to obtain time-accurate results, the computational physical time step is set to be 1.0×10^{-6} s. The non-slip adiabatic wall condition is adopted for the wall, and the outflow boundary condition extrapolates the boundary state from the interior cells. The freestream conditions are adopted for the inflow boundary, and the freestream conditions are $Ma_\infty = 7$, $Re_\infty = 8.61 \times 10^5$ /m, $p_\infty = 392$ Pa, and $T_\infty = 228$ K. The sketch for the computational domain indicating all the boundary conditions is shown in Fig. 3. In addition, laminar flow assumption is adopted in the present study because of the small Reynolds number of flow conditions. Moreover, previous studies in the literature have shown that the numerical simulations of laminar flow in two-body models agree well with wind tunnel tests [20,36–38], and the
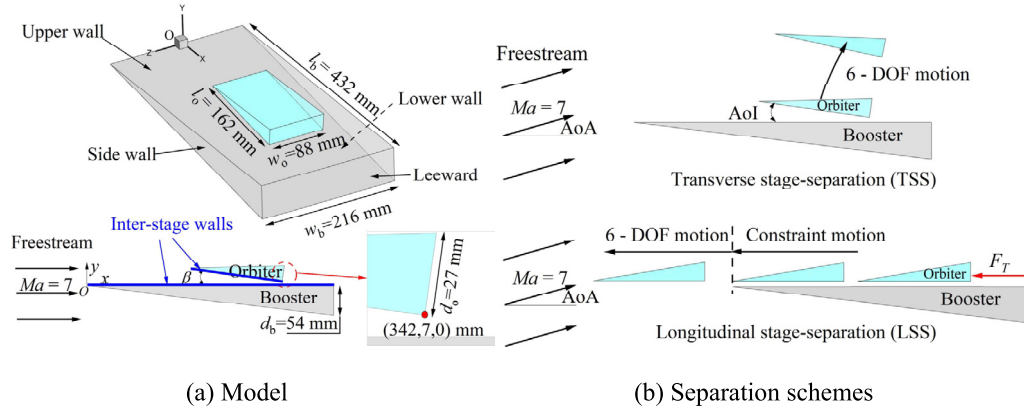
(a) Model

(b) Separation schemes

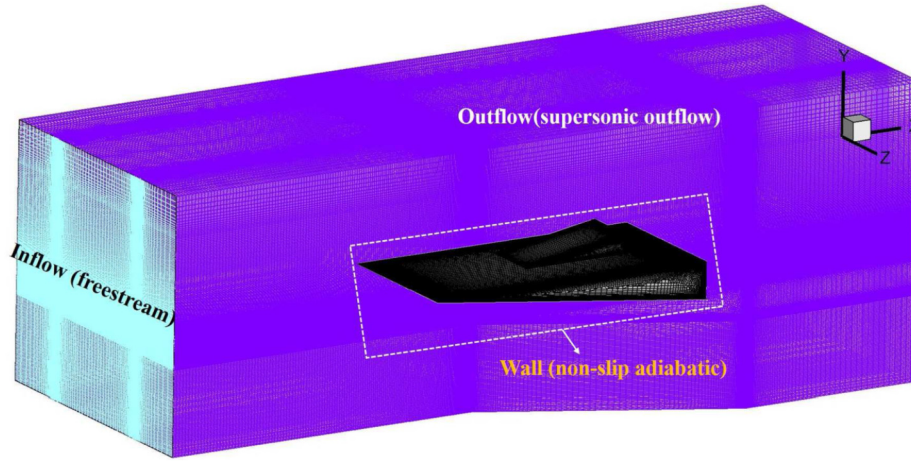**Fig. 2.** TSTO model and separation schemes in the present study.

Fig. 3. Sketch for the computational domain indicating all the boundary conditions.

flow parameters considered the flow over two-stage system can be assumed laminar [3]. Besides, the overset grids technique is used, and N-S equations coupled with 6-DOF rigid body dynamic (RBD) motion equations [39,40] are solved for TSTO dynamic separation. As for the 3-D flowfield postprocessing, LiutexUTA method is used to describe the vortex structure around TSTO and the current work is accomplished by code LiutexUTA, which was released by Liu at the University of Texas at Arlington [41–44].

As for the 6-DOF RBD of the body, its motion can be decomposed into a translation of the CG of the body and a rotation about a body axial system [40]. The dynamic equations of the CG in the body axial system are written as

$$m\left(\frac{dV_x}{dt} - V_y\omega_z + V_z\omega_y\right) = F_x \tag{5}$$

$$m\left(\frac{dV_y}{dt} - V_z\omega_x + V_x\omega_z\right) = F_y \tag{6}$$

$$m\left(\frac{dV_z}{dt} - V_x\omega_y + V_y\omega_x\right) = F_z \tag{7}$$

Where m is the mass of the body, V_x, V_y, V_z are the velocity components of the body (also the velocity of the orbiter grid, $\mathbf{V}_g$), ω_x, ω_y, ω_z are the components of the angular velocity of the body, F_x, F_y, F_z are the components of applied force exerted on the body, including aerodynamic forces, external forces and gravity forces.

The dynamic equations of the rotation of the CG in the body axial system are written as

$$I_{xx}\frac{d\omega_x}{dt} - \left(I_{yy} - I_{zz}\right)\omega_y\omega_z = M_x \tag{8}$$

$$I_{yy}\frac{d\omega_y}{dt} - (I_{zz} - I_{xx})\omega_z\omega_x = M_y \tag{9}$$

$$I_{zz}\frac{d\omega_z}{dt} - \left(I_{xx} - I_{yy}\right)\omega_x\omega_y = M_z \tag{10}$$

Where I_{xx}, I_{yy}, I_{zz} are the principal moment of inertia of the body, M_x, M_y, M_z are the components of applied moment exerted on the body.

The initial position of the orbiter is given at the proper AoI presented in Table 1 in the dynamic separation, and the end position of the orbiter is governed by the 6-DOF RBD equations until the overset grid can not be generated successfully, e.g., the collision occurs or the orbiter grid intersects with the outer boundary of the booster grid. After the aerodynamic forces and moments are obtained using flow solver, the linear and angular displacements of the orbiter can be updated by numerically integrating Eqs. (5)-(10) using 4th order Runge-Kutta scheme. Then, the new position of the orbiter and its grid are updated. After obtaining the position of the orbiter grid using 6-DOF RBD equations at every time step, the computational overset grid at this time step should be generated by overset grid methods, which will be introduced in the next section. The residual criterion for the internal iteration termination is set to 10^{-3} at every time step to guarantee the convergence. Then the new aerodynamic force and moments are obtained again by flow solver and continue to cycle until the end of the computation. The solving procedure can be drawn as the flow chart as shown in Fig. 4.
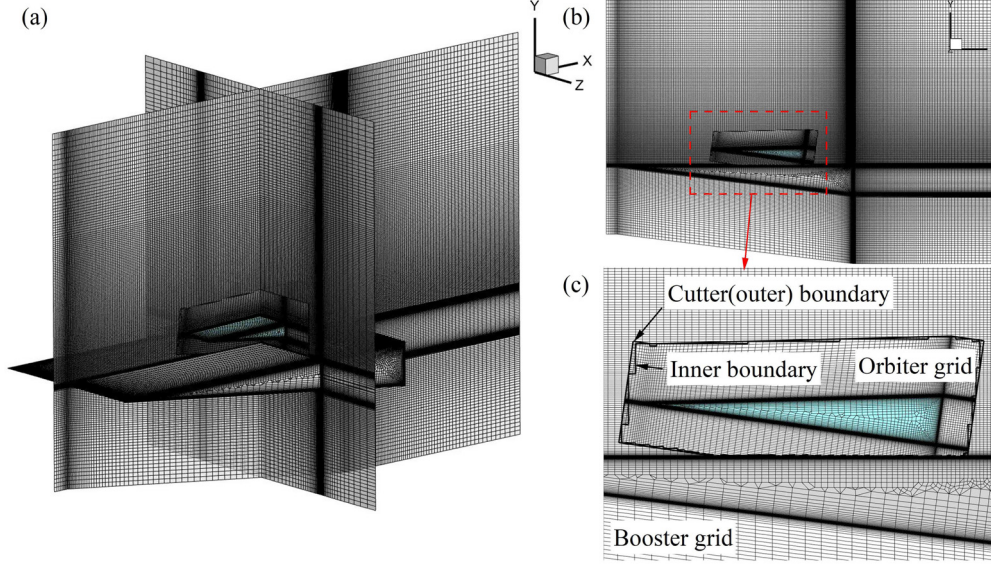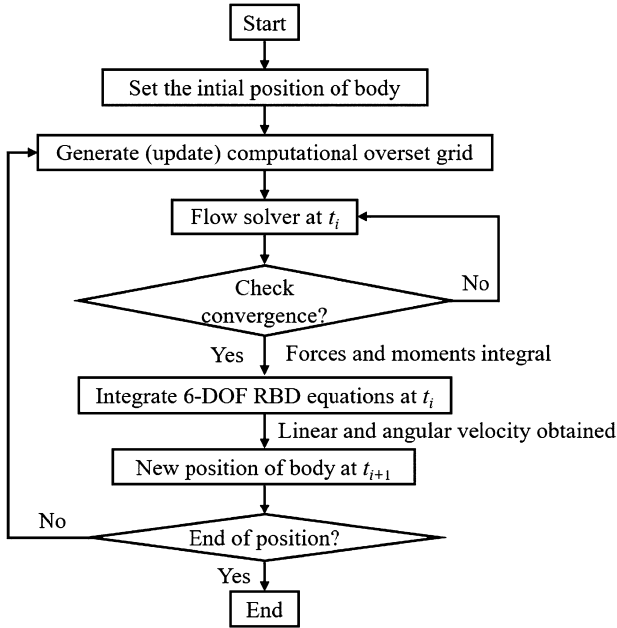
Fig. 5. Computation grids.

Fig. 4. The solving procedure of the TSTO dynamic separation issue.

3.2. Overset grid and grid independency

Given the advantages of the overset grid method and its efficiency in dealing with the multi-body separation problem [39,45], the overset grid technology is adopted to compute the unsteady flow of dynamic separation of TSTO-like two-body system. Fig. 5 (a) shows the perspective view of the computational overset grid with wall grid of stages and slice grids in XY plane and YZ plane, and Fig. 5 (b) shows the side view of the computation grid, and Fig. 5 (c) shows the overset grid boundary of two sub-grids of enlarged view of Fig. 5 (b). As shown in Fig. 5 (a), the 3-D computational grid is composed of a booster grid and an orbiter grid. Both grids are created based on the hybrid meshing approach. Hybrid grids contain structured and unstructured blocks and use hexahedral prismatic cell types. Moreover, special care is taken to ensure smooth cell size progression on all block boundaries. The region near the wall is gridded using boundary layer mesh, and

the first cell spacing normal to the wall is chosen to ensure an average $y^+ < 5$ to capture an appropriate boundary layer flow.

In terms of overset grid techniques, the grids are connected by hole-cutting and data-interpolation, as shown in Figs. 5 (b) and (c). The outer boundary of the orbiter grid is set as the cutter boundary, and the cells that intersect the cutter boundary are identified as the cutter cell. Then, the cutter cell is taken to cut the cells of the booster grid that point to the orbiter grid, thus forming the inner boundary of the booster grid. Moreover, the cutter (outer) boundary and the inner boundary form the overset area of two sub-grids. Therefore, the flow information of two sub-grids is exchanged and interpolated on the overset grids, and the second-order accuracy solution can be achieved with two layers of interpolation grid points. The detailed construction steps of the overset grid can be found in related literature [39]. Besides, the cell size of each sub-grid at the overset zone is close to avoid the discontinuity of the flowfield caused by the difference in grid size. By coupling the 6 – DOF dynamic motion and flow solver, the grid moves with the body, and the overset grid is generated at every time step. Then, the flow information is exchanged between sub-grids to complete the flowfield solution at this time step.

In this study, three grid numbers are used to verify the grid independence. The three grid numbers are coarse grid, medium grid, and fine grid, with the number of grid cells of 5 million, 10 million, and 15 million, respectively. Fig. 6 shows the pressure and shear stress distribution of the symmetry line on the upper wall of the booster at AoI = 8° before stage separation for three computation grids. Fig. 7 shows the displacements and pitching angle, forces and moment of the orbiter in the transverse stage separation case of AoI = 8° for three computation grids. All curves of the three grid numbers are approximately the same in static and dynamic cases. Besides, the medium and fine grids are more consistent at feature points. Thus, considering the accuracy and efficiency of computations, the medium grid is selected for subsequent research and discussion.

3.3. Validation of current CFD code

3.3.1. Test 1: shock wave and boundary layer interaction

Since SBLI is a crucial problem in two-body configurations at high speeds, it is taken as an example. The numerical simulation result is compared with the experiment carried out in Ref [46]. The experiment investigated an oblique shock wave and laminar
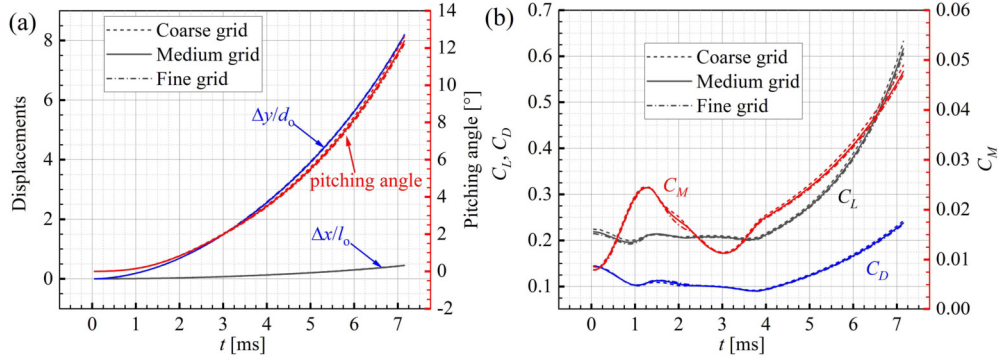
Fig. 7. Displacements and pitching angle (a), force and moment (b) of the orbiter of the dynamic cases in three computational grids.
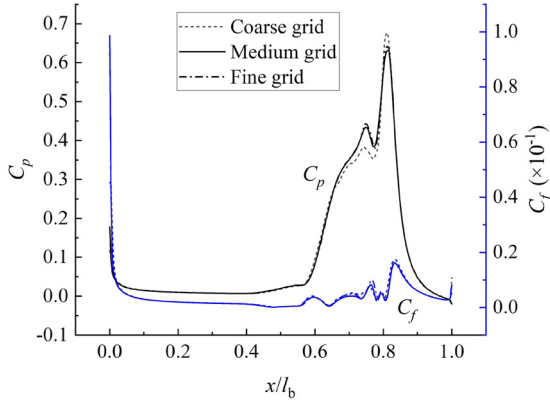

Fig. 6. Grid convergence study (pressure coefficient (C_p) and friction coefficient (C_f) on the upper surface of the booster in three computation grids).

boundary layer interaction at Mach 2.15 and unit Reynolds number 1.2×10^6 /m. More experimental details are depicted in Ref [46]. As shown in Fig. 8, the computed plate streamwise pressure data p/p_0 agrees well with the date measured by the experiment. The computed overset grid and numerical schlieren (contours of $|\nabla \rho|$) are shown in Fig. 8.

3.3.2. Test 2: 3-D wing-pylon-store separation

The wing-pylon-store separation is one of the standard experiment cases to verify the numerical simulation capability of the multi-body relative motion [47,48]. The wing-pylon-store configuration consists of a delta wing and a store. The delta wing has a NACA64A0016 airfoil section with a 45° leading-edge sweep angle. The root chord, semi-span, and taper ratios of the wing are 7.62 m, 6.6 m, and 0.133, respectively. The store diameter is 0.51 m, the length is 3.02 m, and the distance from the store nose to the CG is 1.42 m. Moreover, the store mass is 907.8 kg, and the moments of inertia are $I_{xx} = 27.12$ kg·m^2, $I_{yy} = I_{zz} = 100$ kg·m^2. The basic configuration of the wing-pylon-store is shown in Fig. 9 (a), and the detailed geometry information is depicted in Refs. [11,47]. Fig. 9 (b) shows the hybrid grid (structured and unstructured grid) used for computation, and the number of grid cells is 8.5 million. The inviscid unsteady supersonic flow of 3-D wing-pylon-store dynamic separation is computed by coupling the 6-DOF motion equations based on the overset grid technique. The freestream conditions are $Ma = 1.2$, $Re = 7.87 \times 10^6$ /m, and AoA = 0°. In the computation and wind tunnel test, two ejectors are used to rapidly accelerate the store away from the pylon and to counter the nose-down pitching moment of the store for safety separation. The force of the ejector acting on the store is vertically downward. The forward ejector force of 10679.4 N is applied at 1.24 m from the store nose, and the aft ejector force of 42717.5 N is at 1.75 m from the store nose. Moreover, the ejector stroke length is 0.1 m. Fig. 9 shows the displacements and the Euler angles of the store during separation. The inviscid computational results agree well with the wind tunnel test.

The above two tests reveal that the coupled CFD/6-DOF solver based on the overset grid in the present study can accurately simulate the complex aerodynamic interference and multi-body separation. Also, it can be applied to predict the aerodynamic performance of the stage separation for TSTO systems.

4. Results and discussion

4.1. Transverse stage separation (TSS)

4.1.1. Flow mechanism and aerodynamic characteristics of TSTO before separation

In terms of TSS for the current TSTO model, the orbiter can form an angle of incidence relative to the booster. Therefore, with the SBLI between stages, the orbiter can be vertically separated from the booster under the positive lift. For simplification, the AoA of freestream is set as zero in all TSS cases, so the effect of AoI on the aerodynamic TSS is the only consideration when the influence of AoA is eliminated.

At the initial stage before TSTO separation, the aerodynamic interference is so important that it determines the performance of stage separation, as it has a significant influence on the subsequent forces and moments on TSTO. The interference load (ΔC_L) is an important indicator for evaluating the intensity of aerodynamic interference. It is defined as the difference between the stage loads in stage separation and those for the isolated stage at corresponding AoA of freestream due to the disturbance flowfield (e.g., $\Delta C_L = C_L - C_{L,\text{iso}}$). Fig. 10 presents the interference load of booth stages in different AoI cases. The result shows that the interference load of stages increases with the increase of AoI, indicating that aerodynamic interference becomes stronger and more complex with the increasing AoI. Additionally, since the interference load of the orbiter is greater than that of the booster, the aerodynamic interference received by the orbiter is stronger than that of the booster.

Fig. 11 shows the flow structure and the interstage wall pressure distribution on the centerline. Fig. 12 presents the limiting streamlines of interstage wall (i.e., skin-fraction lines) topology at different AoI cases. As shown in Figs. 11 (a) and 12 (a), in the case of AoI = 0, the boundary layer on the upper wall of the booster with supersonic speed impinges on the orbiter nose forms a leading-edge shock wave S2 and a weak shock wave. The weak shock is reflected on the upper wall of the booster, resulting in the SBLI. Thus, the wall pressure near the interaction zone increases, and a small recirculation zone is induced on the upper wall of the booster. The recirculation zone is an open bubble consisting of a
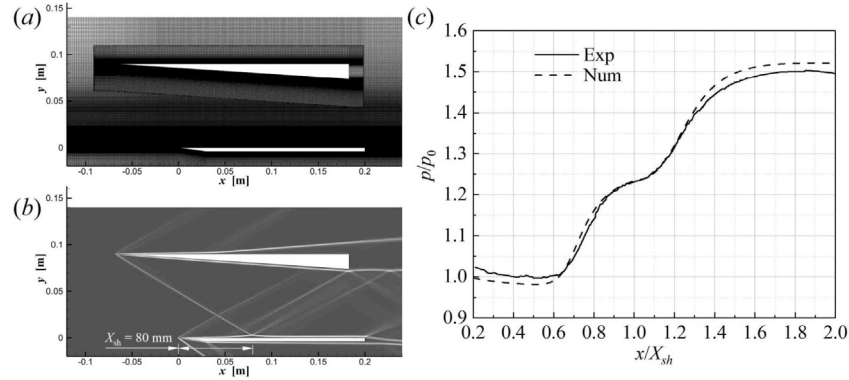
Fig. 8. Shock wave and laminar boundary layer interaction: (a) grid, (b) numerical schlieren (contours of $|\nabla\rho|$) of the flowfield, and (c) streamwise pressure distribution on the plate: numerical and experimental results.
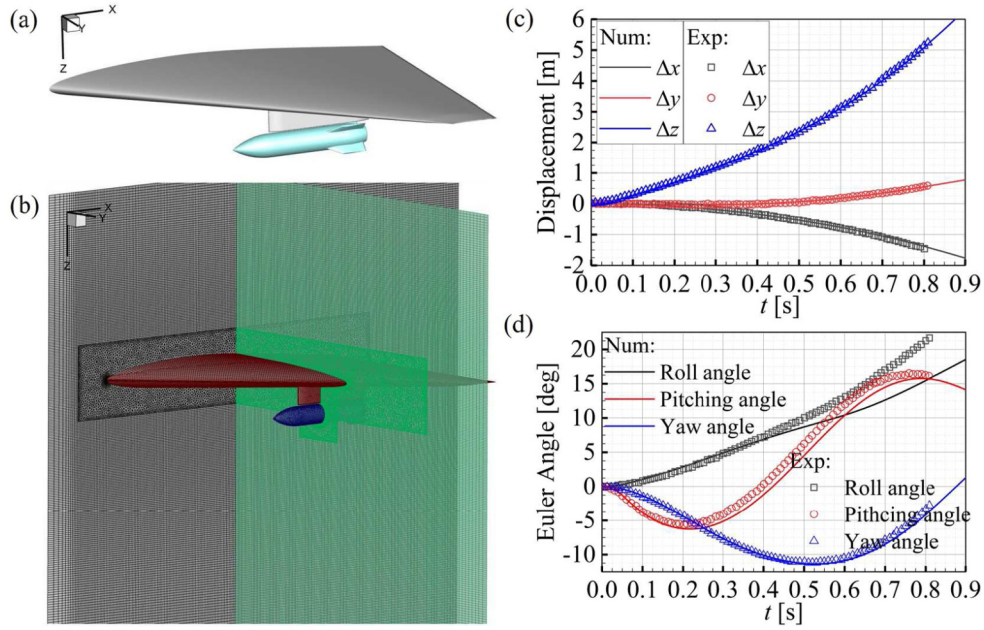

Fig. 9. Wing-pylon-store separation: (a) geometry; (b) grid; (c) and (d) are the numerical and experimental results of linear and angular displacements of the store, respectively.
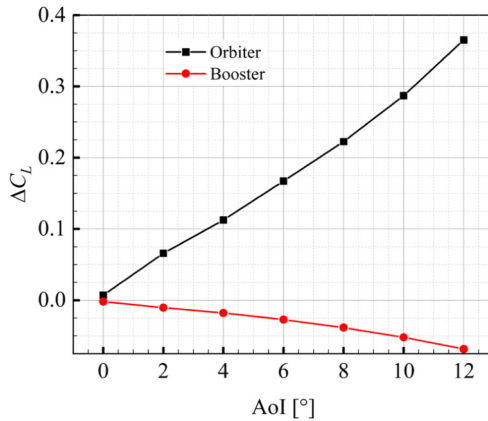

Fig. 10. Interference loads (ΔC_L) of the orbiter and booster.

separation line (S) that originates at S (separation saddle point) and an attachment line (A) that originates at A (attachment node). The recirculation zone is small because of the weak SBLI, close saddle point and node, and no recirculation zone on the lower wall of the orbiter.

With the increase of AoI, the main flow structure of TSTO is not changed, except for the attachment vortex on the leeward of stages gradually separating from the initial convergence state due to the change in the outlet flow state of clearance between stages. Furthermore, the compression shock wave in the wake of the orbiter interacts with that of the booster. The intensity of that interaction increases, and the position of interaction moves downstream. Finally, a reflected shock is formed and interacts with the wake of the orbiter, as shown in Fig. 11 (d). Regarding the flow interference in clearance, the intensity of the shock wave attached to the lower wall of the orbiter increases when the AoI increases to 2°. Therefore, the recirculation zone on the upper wall of the booster becomes larger, and the attachment node is away from the separation saddle point. Moreover, the recirculation zone in 3-D separation flow exhibits as a side vortex around the orbiter and extends downstream. Additionally, the shock wave attached to the lower wall of the orbiter interacts with the booster boundary layer, resulting in cluster compression and expansion waves. The compression waves do not converge into shock waves. The compression and expansion waves are reflected in clearance, repeated several times and ending at the outlet of clearance, causing the pressure distribution on the interstage wall in the shape of alter-
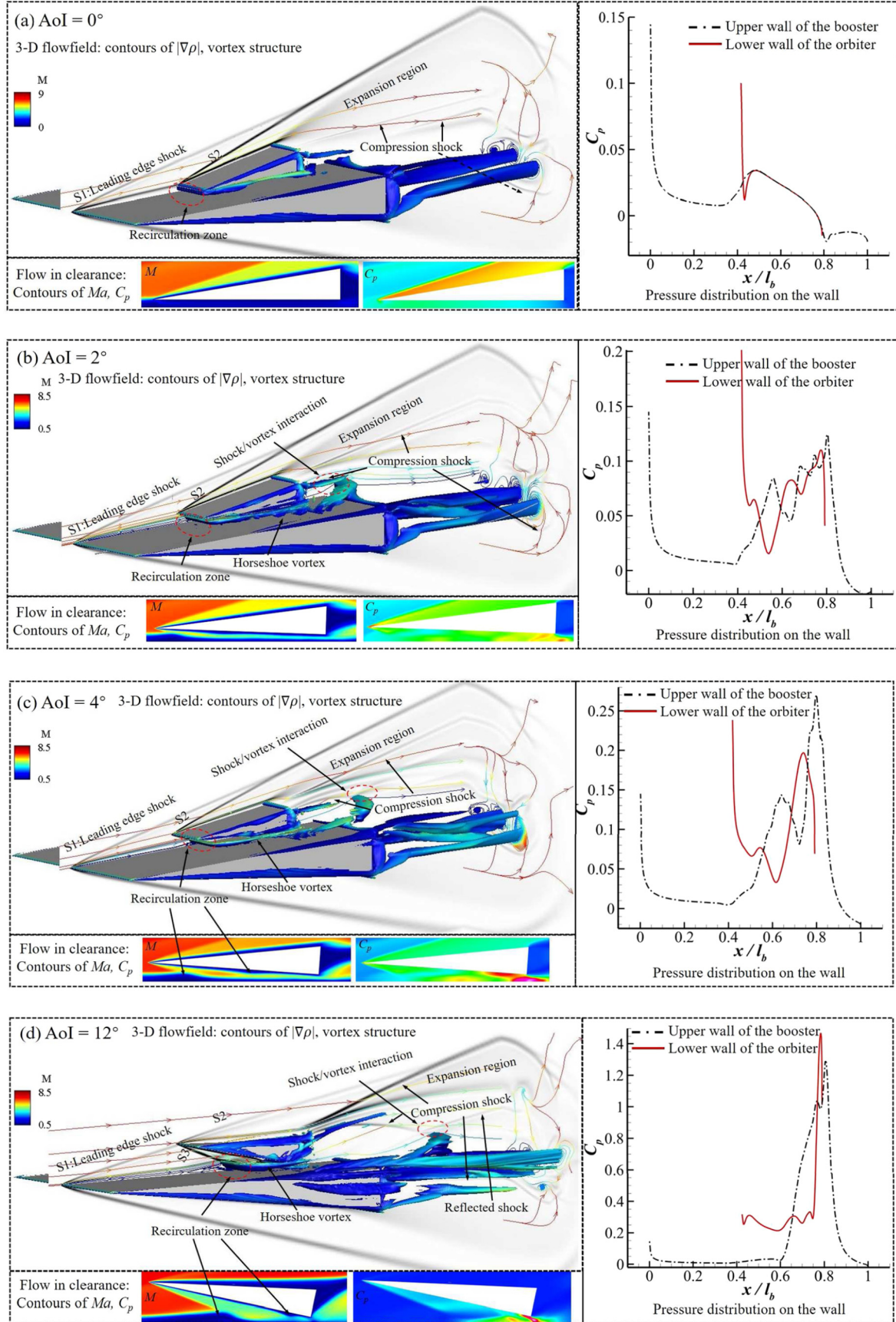
Fig. 11. Typical flow structure illustrated by the numerical schlieren (contours of $|\nabla\rho|$) and iso-surface of Liutex magnitude = 20000 and by streamlines colored by Mach number (upper left), contours of Mach number, pressure of the flow in clearance (lower left), and pressure distribution of centers line on the wall (right).
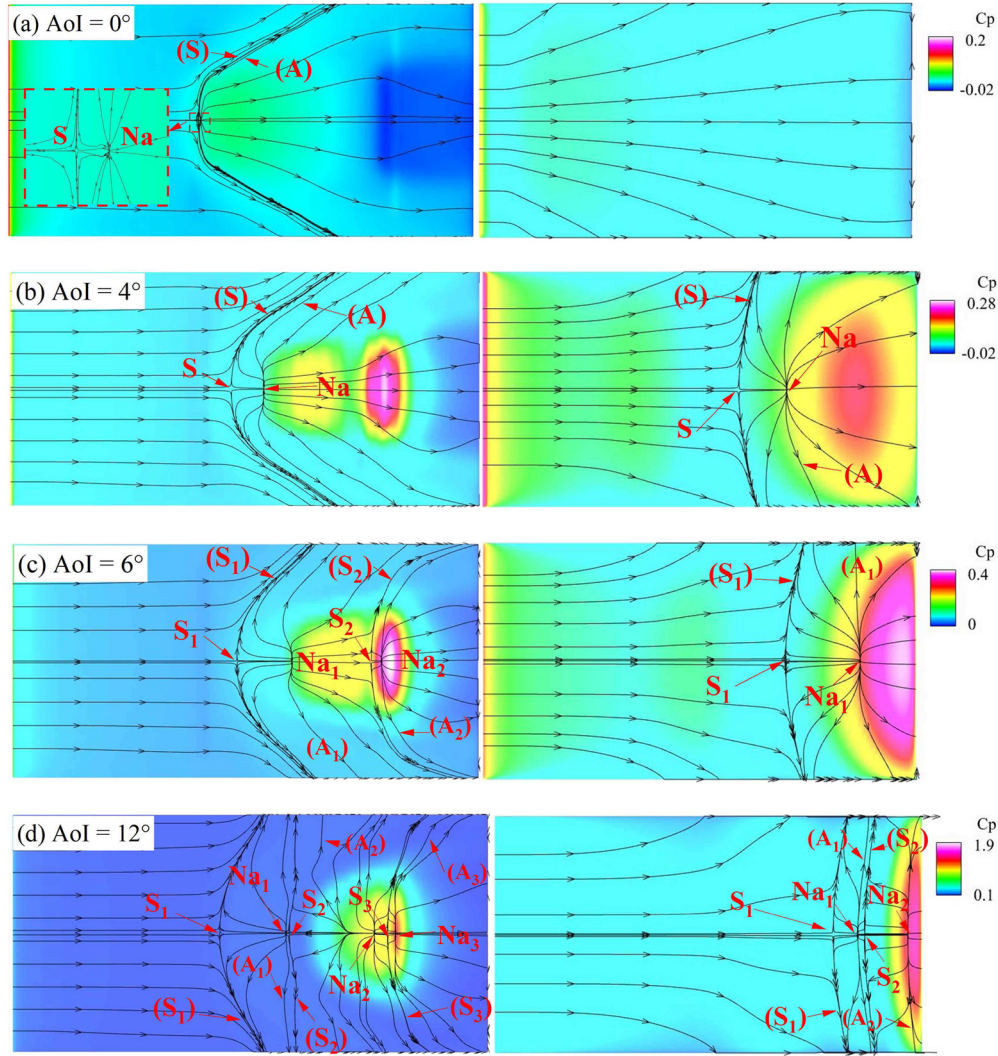
Fig. 12. Pressure contour distribution of interstage walls with limiting streamlines: the upper wall of the booster (left) and the lower wall of the orbiter (right).

nating peaks to valleys in clearance, as illustrated in Fig. 11 (b). However, the pressure rise caused by the compression waves in clearance is not sufficient to separate the boundary layer, so no secondary separation flow occurs in clearance and the topology of the limiting streamline is not essentially changed.

When the AoI increase to 4°, the pattern of compression and expansion waves reflected in clearance changes into the reflection of the shock wave in clearance, namely, SBLI occurs. From the pressure curves shown in Fig. 11 (c), the SBLI in clearance results in an apparent pressure rise. The trend of the pressure curve shows that two SBLI occurs on the booster and orbiter, respectively. Moreover, the SBLI on the orbiter induces the flow separation on the lower wall, resulting in a separated topology composed of a separation saddle point and attachment node. Because of the intensity of interference, the recirculation zone on the upper wall of the booster enlarges, and the attachment node moves downstream, as shown in Fig. 12 (b). When the AoI increases to 6°, as the intensity of interference further increases, the SBLI occurs on the lower wall of the orbiter, causing the reattachment shock wave to impinge on the upper wall of the booster and induce a secondary flow separation. As shown in Fig. 12 (c), separation line (S_1) separates the skin-friction lines originating upstream from that originating at attachment node N_1 situated behind S_1, and the second saddle point S_2 exits downstream of S_1 and Na_1 with a secondary separation line (S_2). Thus, there are two pairs of the saddle – attachment

node on the upper wall of the booster, and the recirculation zone in clearance moves downstream as it becomes larger.

With further increase in AoI, the flow structure and topology of separation flow are not change despite increasing interference intensity. However, when the AoI increases to 12°, the strong aerodynamic interference induces a notable pressure rise in clearance (as shown in Fig. 11 (d)), and the topology of 3-D separation flow is more complicated. As shown in Fig. 12 (d), when the first recirculation zone becomes larger, the separation saddle point S_1 moves upstream and the second separation flow is formed behind the attachment node Na_1 with the separation saddle point S_2 and attachment node Na_2. Because of the reattachment of the secondary separation flow, the induced reattachment shock wave impinges on the orbiter and causes SBLI, resulting in the first separation flow (i.e., the saddle point S_1 and node Na_1) on the orbiter. Similarly, the reattachment of the separation flow on the orbiter leads to a third separation flow on the booster $(S_3$ and $Na_3)$ at the outlet of clearance, and the third separation flow induces the secondary flow separation on the orbiter.

Fig. 13 presents the aerodynamic coefficients of the orbiter and booster at different AoI cases. With the increase of the AoI, the aero force and moment of the orbiter are increased, with the aerodynamic interference intensity becoming stronger. Due to the high-pressure zone on the lower wall of the orbiter moving downstream with the increasing AoI, the increasing rate of the pitching
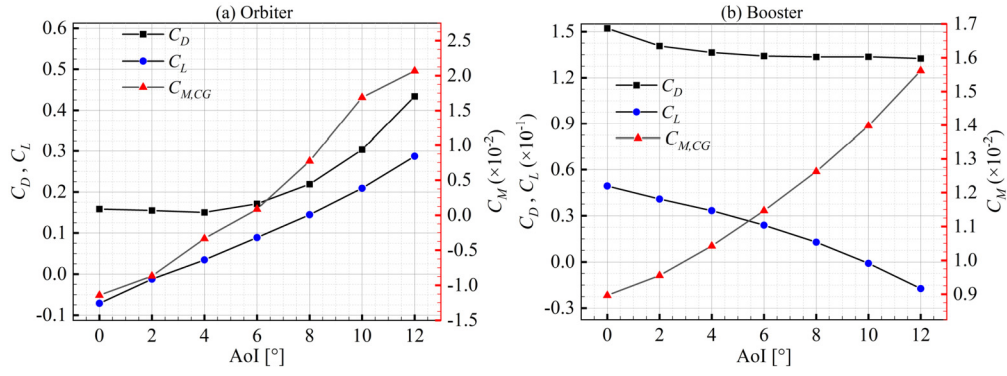
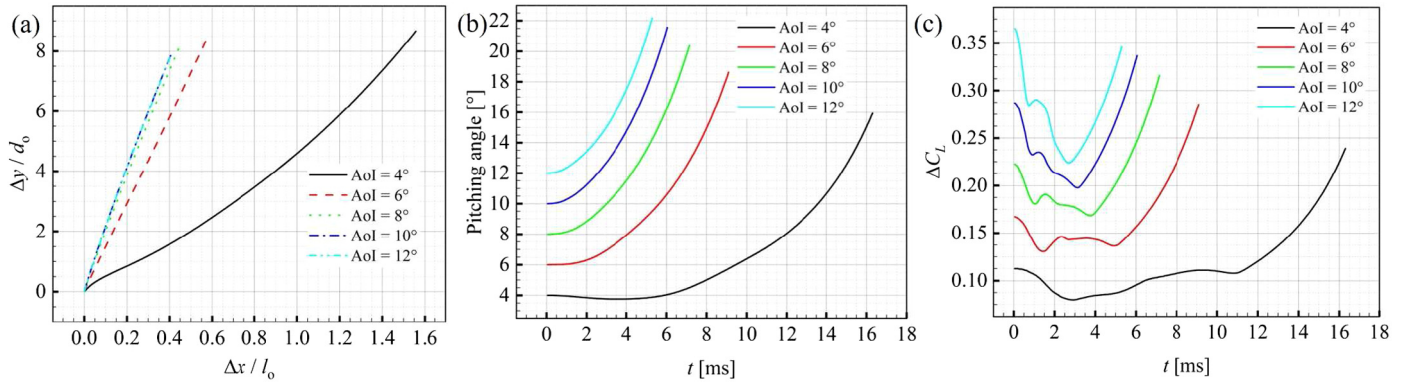**Fig. 13.** TSTO aerodynamic characteristics with different AoI values.

Fig. 14. Displacement (a), pitching angle (b), and interference load (c) of the orbiter during TSS in different AoI cases.
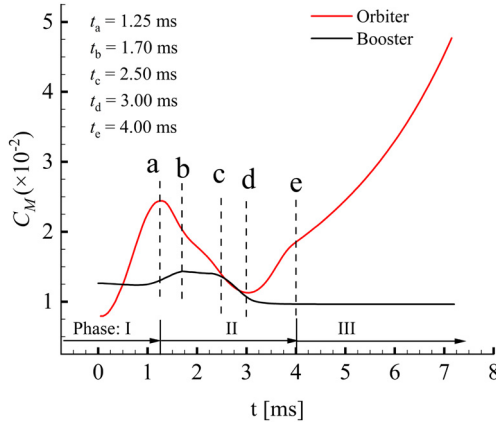

Fig. 15. Time history of the pitching moment during TSS in the case of AoI = 8°.

moment is larger than that of lift. As shown in Fig. 13 (b), the drag of the booster does not change obviously with the variety of AoI, while the lift decreases and the pitching moment increases due to the downstream moving of the high-pressure in clearance. Furthermore, the lift and pitching moment of the orbiter is a negative value when AoI < 2° and AoI < 4°, respectively. Therefore, the case of AoI < 2° is not conducive to the stage separation, and the orbiter will collide with the booster under the combined action of the negative lift and nose-down moment. Thus, the TSS case when AoI ≥ 4° is discussed in the next section.

4.1.2. Flow mechanism and aerodynamic characteristics of stage separation

The unsteady flow of aerodynamic TSS of TSTO is simulated by coupling the 6 - DOF motion equations based on the overset grid technique. In the computations, the orbiter is freely released

without any momentum, whereas the booster is fixed to provide a stable aerodynamic environment for stage separation. As discussed in the previous section, the aerodynamic coefficients of the booster varies less than those of the orbiter. Therefore, the booster is assumed to keep its flight status to reduce the influence on the orbiter during stage separation. Fig. 14 presents the displacement, pitching angle, and interference load of the orbiter during stage separation in different AoI cases. As shown in Figs. 14 (a) and (c), with the increase of AoI, the interference loads will be stronger on the orbiter, and the displacement of the orbiter will be greater. In other words, the separation time of TSTO is shorter in larger AoI cases. In addition, the pitching angle of the orbiter increases faster in larger AoI cases due to the stronger pitching moment, as shown in Fig. 14 (b). Moreover, the trend and value of displacement and pitching angle curves for the orbiter are similar in the cases of AoI > 6°, which reveals a similar flow structure and aerodynamic interference between stages during stage separation. For the case of AoI = 4°, due to the action of the nose-down pitching moment and small lift, the separation time for the orbiter is relatively long, which is not ideal for stage separation. The representative case of AoI = 8° for TSS is analyzed as follows.

Fig. 15 illustrates the pitching moment of stages during separation in the case of AoI = 8°. The whole separation process can be divided into three phases: I - small clearance flow, II - large clearance flow, and III - no interference flow. In terms of phase I, strong aerodynamic interference and complex separation flow topology exit in clearance before the orbiter nose pass through the leading-edge shock of the booster, and the interference loads increase rapidly. When the orbiter nose passes through the leading-edge shock, the flow enters phase II, and SBLI plays the main role in the flow. When the leading-edge shock does not impinge on the lower wall of the orbiter, the flow enters phase III. There are no interference loads on the stages, and the flow interference is domi-
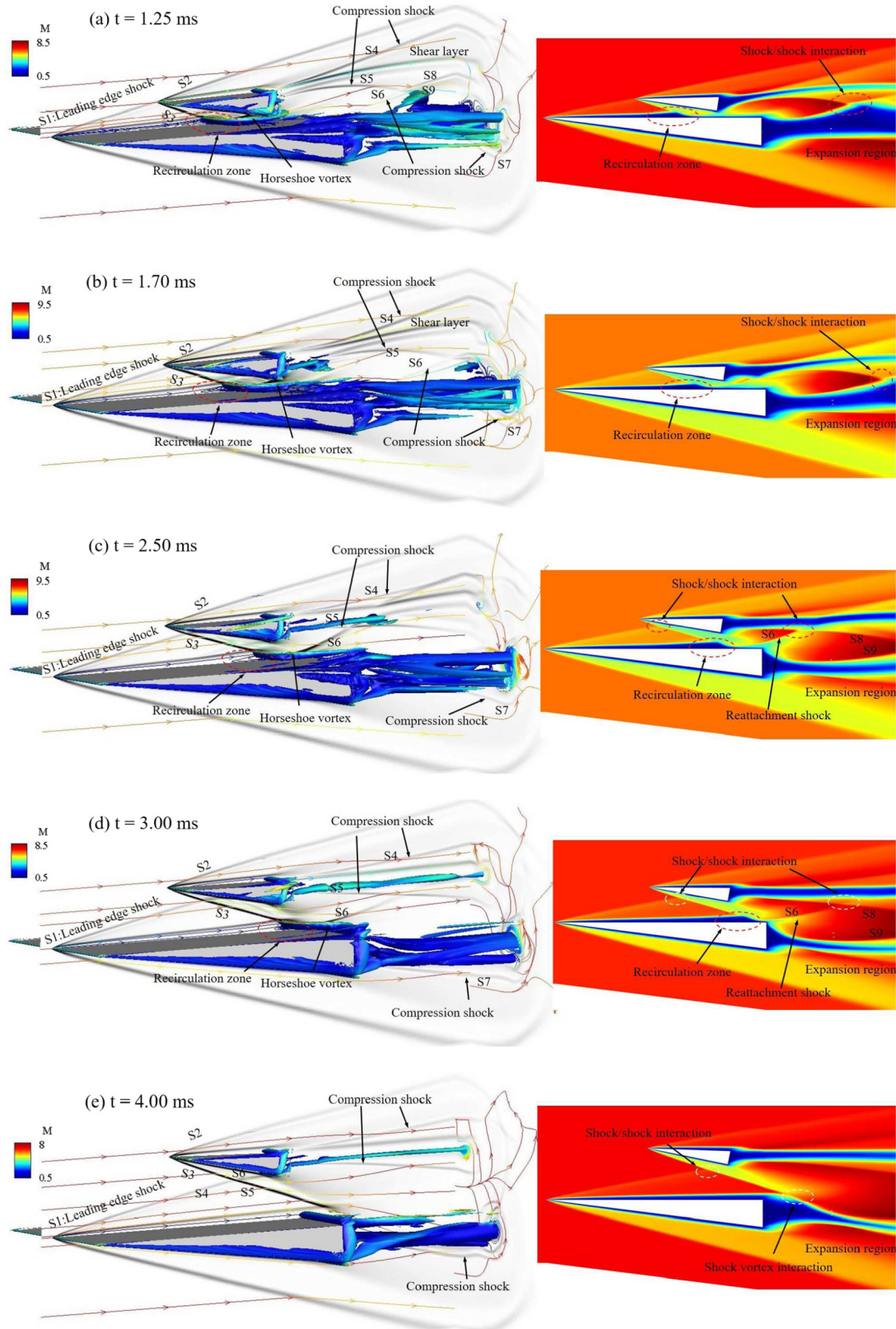
Fig. 16. Flowfields illustrated by the numerical schlieren (contours of $|\nabla \rho|$) and iso-surface of Liutex magnitude = 15000 and streamlines colored by Mach number (left) and contours of Mach number (right) of different instants during TSS in the case of AoI = 8°.

nated by the interaction between the leading-edge shock wave and the wake flow. Then, the stage separation of TSTO is completed.

Fig. 16 shows the flowfield of different instants labeled in Fig. 15 during TSS in the case of AoI = 8°. In phase I, the intensity

of aerodynamic interference in clearance decreases slightly with the increase of clearance, causing the pressure on the lower wall of the orbiter and aero forces acting on the orbiter to decrease. The leading edge shock wave S3 of the orbiter interacts with the
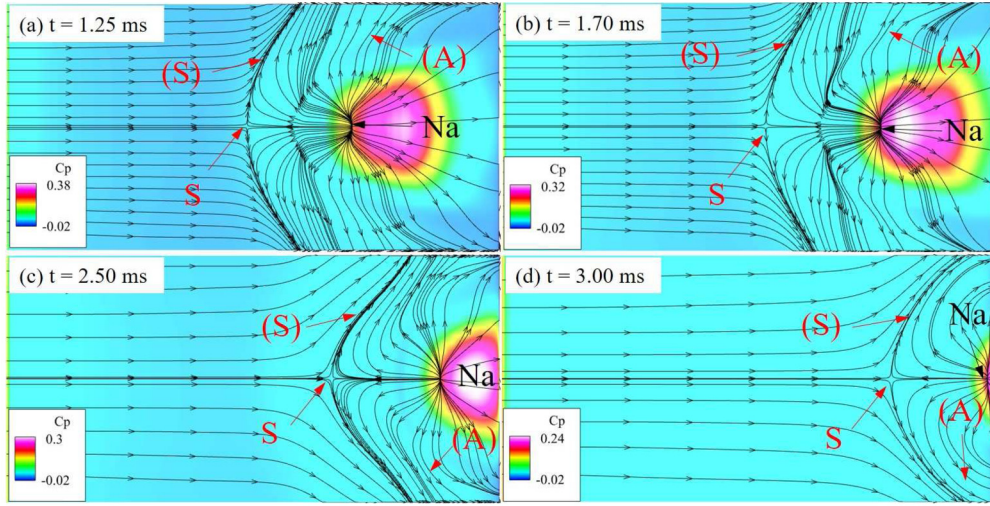
Fig. 17. Pressure contour distribution of upper wall of the booster with limiting streamlines.

boundary layer on the booster, resulting in flow separation on the booster and inducing a reattachment shock wave impinges on the orbiter lower wall. However, with the increase of clearance, the intensity of the interference between the reattachment shock wave and aft body of the orbiter gradually decreases and finally does not impinge on the lower wall of the orbiter at the instant (b). Thus, the high-pressure zone on the aft body of the orbiter decreases and disappears, resulting in a reduction and eventual disappearance of the nose-down induced by high pressure. Moreover, the pressure on the nose rises as leading-shock S1 impinges on the orbiter nose so that the nose-up moment acting on the orbiter reaches its maximum value at the instant (a). Besides, the lift of the booster increase as a result of the decrease in the intensity of aerodynamic interference.

At the instant (b), the position of SBLI on the upper wall of the booster and lower wall of the orbiter moves downstream across the CG, resulting in a decrease and an increase in the nose-up moment of the orbiter and booster, respectively. Moreover, the nose-up moment of the booster is maintained at a high platform, as shown in Fig. 15. Besides, as illustrated in Fig. 16 (b), the reattachment shock wave on the upper wall of the booster interacts with the wake behind the orbiter, resulting in the stretching deformation of the wake vortex. In terms of instant (c), with increasing clearance, the high-pressure zone on the upper wall of the booster caused by SBLI further moves downstream, and the intensity of interference in clearance decreases, leading to a further reduction in the nose-up moment of the orbiter. Besides, type I shock interference occurs when reattachment shock wave S6 crosses compression shock S5 in the wake and induces the transmitted shock wave S8.

At the instant (d), the recirculation zone on the booster arrives at the end of the aft body of the booster, and the reattachment shock wave S6 is about to disappear so that the value of the moment of the booster turns into that of undisturbed state. Furthermore, since the aft body of the orbiter is no longer affected by interference, the pressure distribution reaches the minimum value. Additionally, the position where the leading-edge shock S1 of the booster impinges on the orbiter nose is also moving downstream across the CG to make the nose-up moment of the orbiter reach the minimum value in phase II. Besides, the intensity of reattachment shock wave S6 and the intensity of interference between S6 and S5 in the wake decrease, resulting in a gradual recovery of the deformation of the wake vortex behind the orbiter.

Finally, SBLI does not occur on the booster and recirculation zone, and the horseshoe vortex disappears at the instant (e). The

weak leading-edge shock interacts with the leading-edge shock S3 of the orbiter, resulting in the transmitted shock S6 impinging on the aft body of the orbiter. Then, the flowfield enters phase III, where the orbiter will be completely free from the shock interactions and prepare to into orbit. The stage separation of TSTO finished. In addition, transmitted shock wave S5 interacts with the wake flow, and S6 interacts with the expansion fan near the attachment vortex on the leeward of the orbiter.

As shown in Fig. 17, in terms of the separation flow topology, the topology of the separation flow on the upper wall of the booster variates from the double "saddle point - node" pattern into the single "saddle point - node" pattern with the increasing of clearance. Furthermore, the 3-D recirculation zone (i.e., horseshoe vortex) on the upper wall of the booster moves downstream and decreases gradually. Since the intensity of the interference in clearance decreases, the rise of the pressure on the lower wall of the orbiter does not induce flow separation, and the separated pattern variates from the initial "saddle point - node" pattern into the no separation pattern quickly.

Fig. 18 presents the aerodynamic coefficient curves of the stages during TSS in different AoI cases. The aerodynamic variation of the stage corresponds to the above flowfield analysis. As shown in Fig. 18, the trend of the aerodynamic coefficient curve is similar to that of other cases in different AoI cases, which again indicates that the physical flow is similar for different AoI cases. Moreover, the aerodynamic variations of stages during separation in the cases of $6° \leq AoI \leq 8°$ are relatively stable compared with those in the cases of $AoI > 8°$, and the interference loads are smaller. As illustrated in Fig. 18 (b), in terms of the separation time (i.e., the time from the beginning of separation to phase III), the separation time decreases with the increase of the AoI when $AoI \leq 10°$ and reaches the critical value at $AoI = 10°$. Namely, the separation time does not further decrease with the increase of AoI when $AoI > 10°$. The separation time is longer when $AoI < 6°$ for the lift of the orbiter is not large enough. An excessively long separation time can increase the uncertainty in the high-speed separation process of TSTO, e.g., the time is almost twice as long for $AoI = 4°$ as for $AoI = 8°$. In short, the AoI of the orbiter at $6 \sim 8°$ may have higher safety and reliability for TSS of the current TSTO model. In a short separation time, the two stages can be separated relatively smoothly without collision, and the orbiter enters the orbit at an appropriate attitude angle.
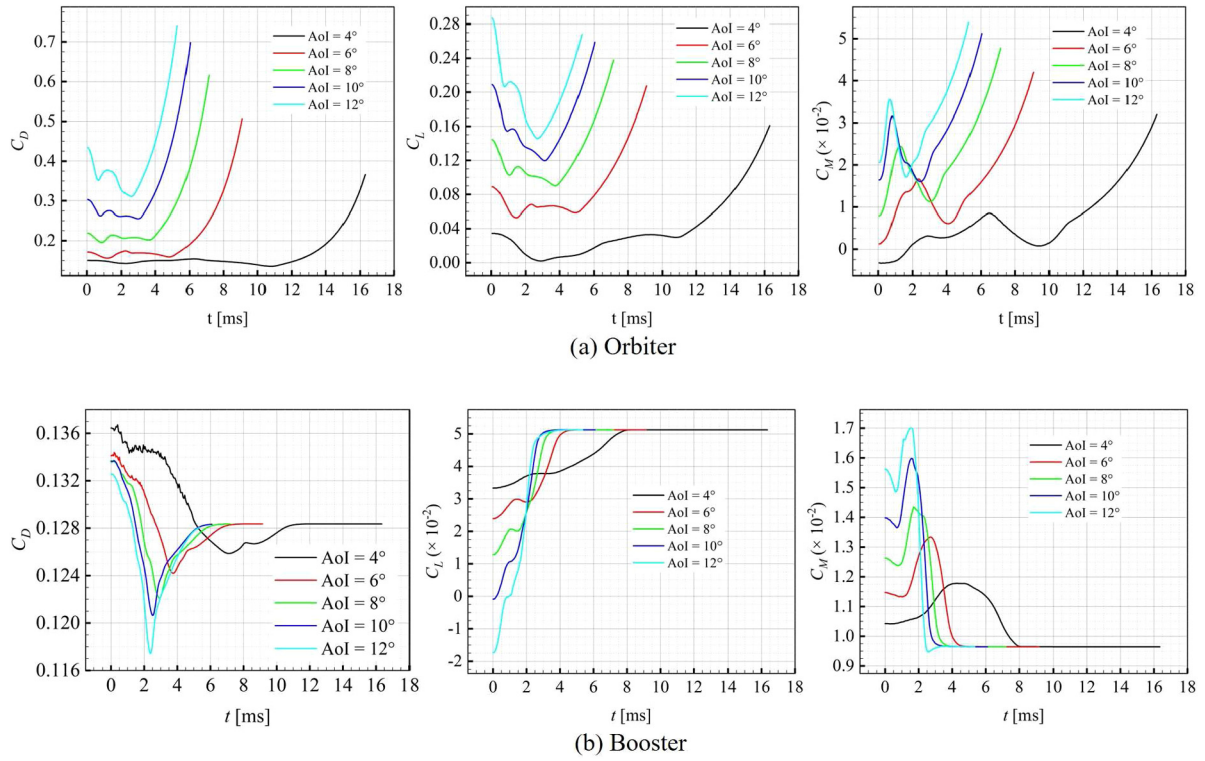
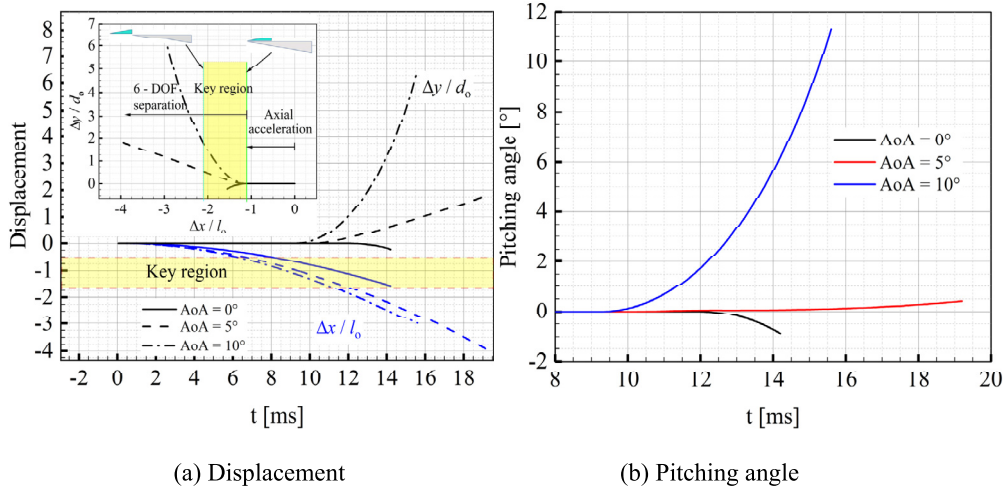Fig. 18. Aerodynamic characteristics of TSTO during TSS.

Fig. 19. Displacement and pitching angle of the orbiter during LSS.

4.2. Longitudinal stage separation (LSS)

4.2.1. Aerodynamic separation characteristics

In terms of LSS, the orbiter accelerates close to the booster until it breaks the leading-edge shock of the booster because of the negative lift at zero AoA condition and supporting force from the booster. Then the orbiter is separated from the booster with proper positive lift and pitching moment if possible. A clear intention is to reduce the influence of the interstage interference on the stage occurring at a large clearance situation in TSS. Hence, the LSS of the TSTO-like parallel arrangement wedges model is numerically studied at AoA = 0°, 5°, 10°, respectively. Besides, the wedge angle of the orbiter model is 9.46°. Moreover, the computation process has been stated in Section 2. As shown in Fig. 19, two stages collide in the key region at $t = 14$ ms in the case of AoA = 0° due to the negative lift and nose-down motion. Conversely, the orbiter safely

separates from the booster when AoA = 5° and 10° because of the positive lift and nose-up motion. Furthermore, the separation time for AoA = 10° is short, although it is dominated by the thrust on the orbiter when there is no collision between stages.

Fig. 20 presents the force and moment of the stages that vary with the displacement of the orbiter during stage separation at different AoA cases. According to Fig. 20, the general variation trend between the forces and moment for the orbiter and booster is approximately the same. For example, the aerodynamics of the orbiter change steadily first and then change notably near the "nose coincidence" position, and finally change stably after the orbiter separates from the booster. In addition, the aerodynamics of the booster fluctuates within a narrow range, while that of the orbiter fluctuates within a spacious range. Namely, the influence of aerodynamic interference on the booster is weaker than that on the orbiter. Therefore, the booster can hold its flight attitude during LSS,
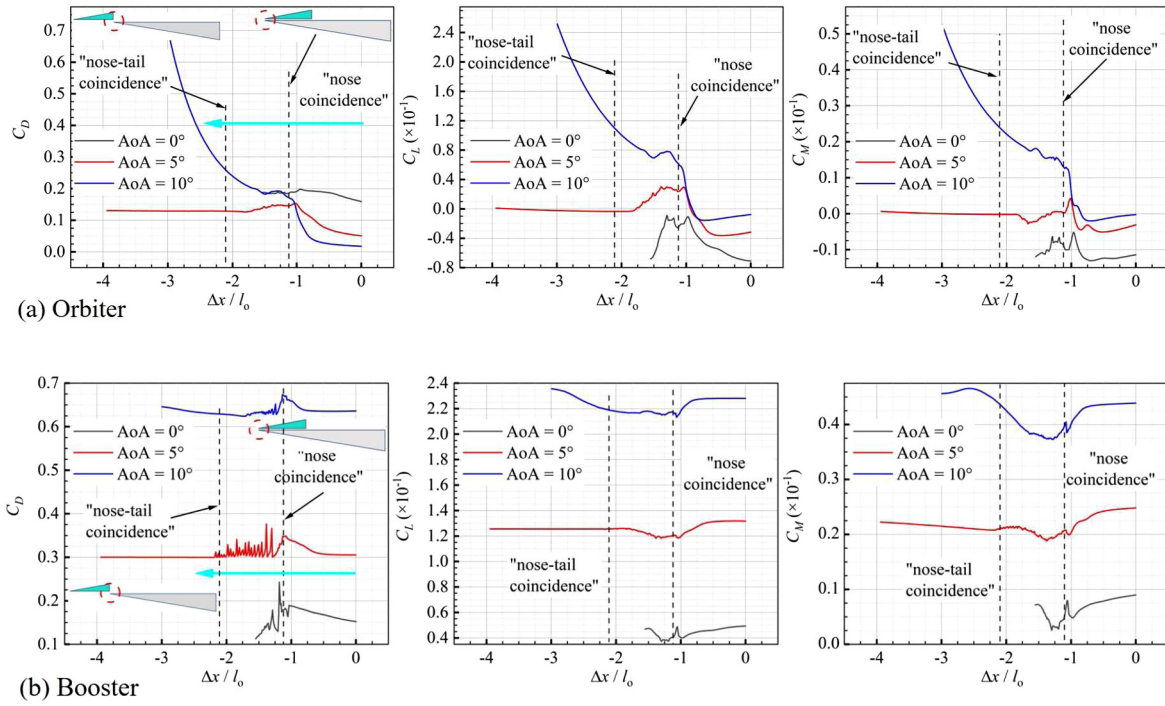
13

Fig. 20. Aerodynamics of the orbiter and booster during LSS.

and the computation assumption of the fixed booster is reasonable. Furthermore, putting aside the AoA = 0° case where the collision occurs, the orbiter is safely separated from the booster with a terminal positive lift and nose-up moment. But, the aerodynamics of both stages show a relatively moderate change in the AoA = 5° case, compared with the AoA = 10° case. Besides, the aerodynamics of both stages increases with the increase of AoA, especially for the AoA = 5° case, where the lift and the nose-up moment of the orbiter are nearly zero, while those behave at a relatively large value in the AoA = 10° case. Hence, the LSS of the AoA = 5° case for the current TSTO model is more favorable since the orbiter separates smoothly without violent aerodynamics change from the booster. The alternative AoA value for the safe LSS could be better near 5° and less than 10°. Since the particularity of AoA = 5° case and flow structure and interference patterns are similar between AoA = 5 and 10° cases before "nose-tail coincidence". Thus, the flow structure and mechanism of interference and the effects on the aerodynamic coefficients during stage separation at AoA = 5° and specific flowfield at AoA = 10° are discussed and clarified in the next section.

4.2.2. Flow structure and mechanism

As presented in Fig. 21, the feature points of the pitching moment of stages in the LSS case of AoA = 5° are labeled, representatively showing the changes of the structure and mechanism of the interference flowfield. Because of the small clearance characteristics of the LSS, the flowfield around the TSTO is predominated by the wake vortex/boundary layer interaction, and SBLI in clearance is very weak.

The flow structure around TSTO at some relative positions or instants labeled in Fig. 21 are sketched in Fig. 22, and corresponding separation flow topologies are sketched in Fig. 23. As sketched in Fig. 22 (a), the flowfield is dominated by the complex vortex systems (i.e., the leading-edge vortex and wake vortex system), and the weak SBLI occurs in clearance. The formation mechanism of the SBLI and orbiter side vortex is similar to the case of AoI = 0° (Fig. 11 (a)) discussed in Section 4.1.1. The wall pressure near SBLI increases and the recirculation zone is induced. In addition,

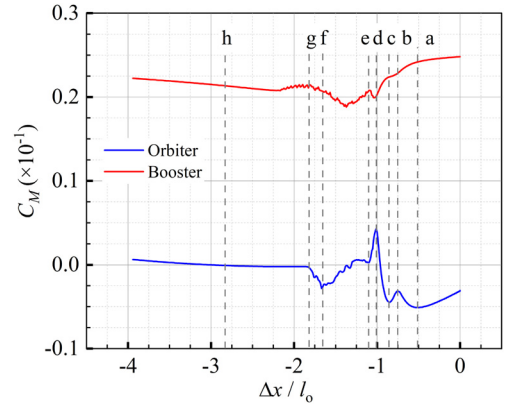Fig. 21. Pitching moment of stages during LSS in the case of AoA = 5°.

a leading-edge vortex pattern occurs on the upper wall of the booster and is created by the following mechanism. The pressure on the lower wall of the booster at AoA is higher than the pressure on the upper wall. Thus, the flow on the lower wall near the sidewall tries to curl around the "shoulder" of the booster, and the flow separates along its entire length. In addition, as shown in Fig. 23 (a), in terms of the separation flow topologies, the recirculation zone is an open bubble consisting of a separation line (S_1) that originates at the S_1 (separation saddle point) and an attachment line (A_1) that originates at the A_1 (attachment node). Moreover, the complex interference of the orbiter wake vortex between the booster boundary layer results in a pair of saddle-spiral stable separated patterns, and an attachment line (A4) corresponding to the leading-edge vortex is also observed. For the aerodynamics of the orbiter, the orbiter nose is submerged in the boundary layer of the booster until the moment (a) when the boundary layer of the booster with high speed impinges on the orbiter nose just right, so that the nose-down moment reaches the maximum value.

When the orbiter moves to position (b), the flow structure and separation flow topology are similar to those at position (a). However, the boundary layer of the upper wall of the booster im-
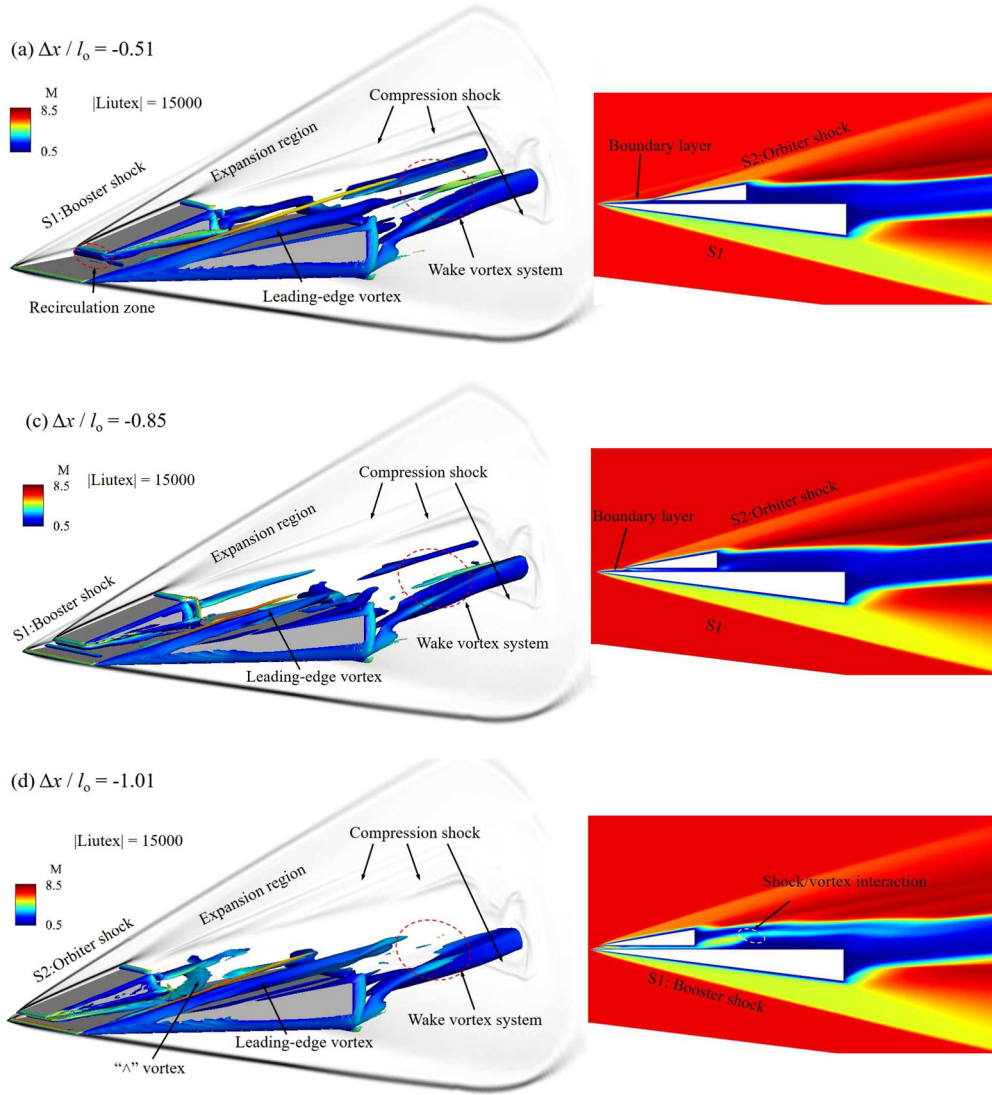
14

(a) $\Delta x / l_o = -0.51$

(c) $\Delta x / l_o = -0.85$

(d) $\Delta x / l_o = -1.01$

Fig. 22. Flowfields illustrated by the numerical schlieren (contours of $|\nabla \rho|$) and iso-surface of Liutex magnitude colored by Mach number (left) and contours of Mach number (right) of different relative positions during LSS in the case of AoA = 5°.

pinges on the lower wall of the orbiter near its nose as the orbiter moves upstream, which contributes a nose-up moment effect on the orbiter, resulting in the nose-down moment of the orbiter to encounter a local minimum value. When the orbiter moves to position (c), as the thickness of the boundary layer decreases, the intensity of the SBLI caused by the orbiter shock is reduced. Hence, the pressure underneath the orbiter nose is slightly increased, and the flow does not separate without a high enough adverse pressure gradient in the boundary layer, as shown in Fig. 23 (c). Moreover, the separation flow behind the orbiter is changed from the saddle-spiral pattern into the node-saddle pattern. Since the weaker SBLI occurs at the orbiter nose, the nose-up contribution effect decreases so that the nose-down moment of the orbiter reaches the local maximum value.

As the orbiter passes through the leading-edge shock of the booster, i.e., at position (d), the leading-edge shock of the booster impinges on the lower wall of the orbiter nose, resulting in the high-pressure distribution. Hence, the moment of the orbiter turns into the nose-up moment and reaches a local maximum value at this moment. Furthermore, the wake of the orbiter separates from the separated boundary layer of the booster, and the compression shock interacts with the separated boundary layer induces a "∧"

vortex, causing the shock/vortex interaction. Moreover, with the interaction of the compression shock, the "∧" vortex is raised, and the saddle point on the upper wall of the booster moves downstream, as illustrated in Fig. 23 (d). As the orbiter further moves upstream, the impinging position of the leading-edge shock on the lower wall of the orbiter is moving downstream relatively so that the nose-up of the moment is decreasing. When the nose of both stages coincides at position (e), the nose-up moment of the orbiter decreases to a platform near-zero value. Besides, the flow structure and separation flow topology are similar to those of position (d) flowfield. In terms of the pitching moment of the booster, the high pressure on the upper wall of the booster moves upstream with the motion of the orbiter, causing the nose-up moment to decrease.

When the orbiter moves to position (f), the pitching moment of the orbiter has turned from the nose-up moment into the nose-down moment, and the nose-down pitching moment reaches a local maximum value. As shown in Fig. 22 (f), the position of SBLI on the lower wall of the orbiter moves downstream of the CG, resulting in the local maximum value of the nose-down moment. Moreover, with the further separation between the wake of the orbiter and upper wall of the booster separated boundary
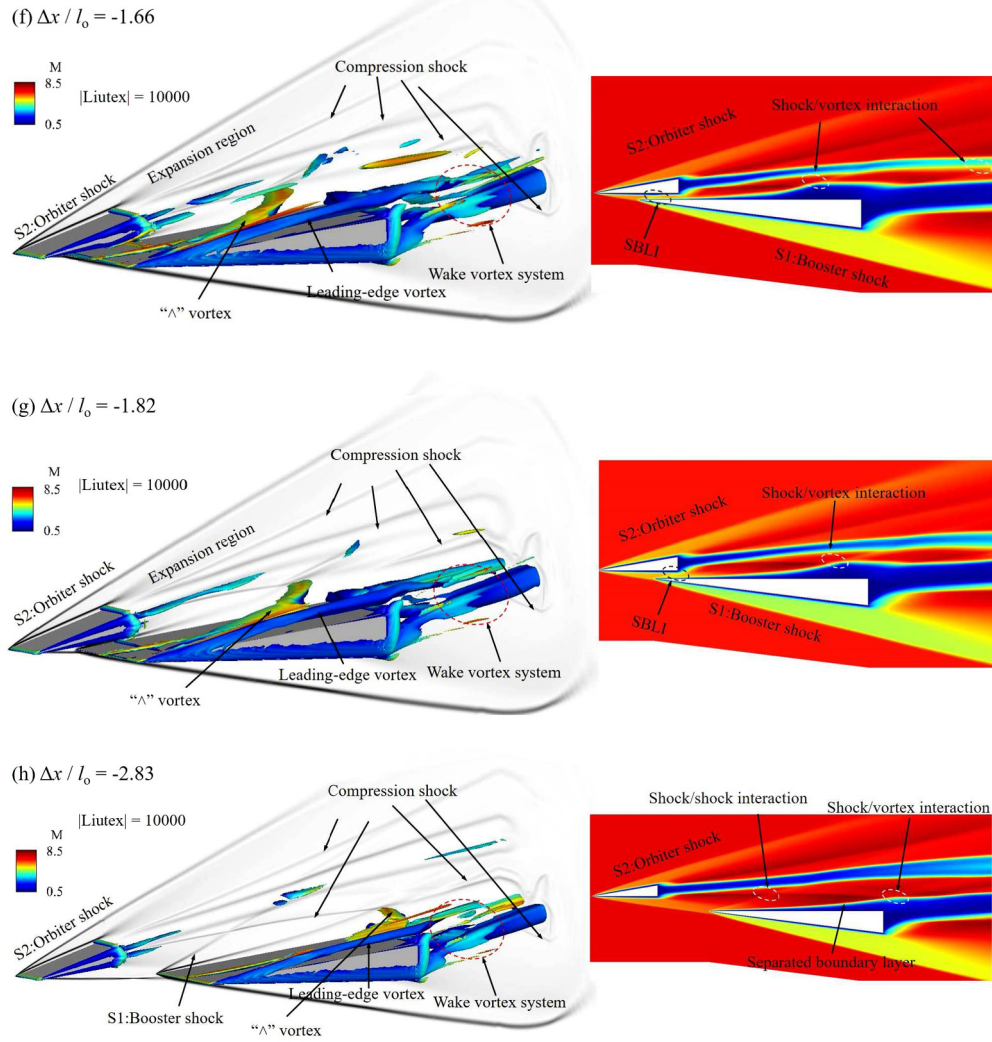
(f) $\Delta x / l_o = -1.66$

(g) $\Delta x / l_o = -1.82$

(h) $\Delta x / l_o = -2.83$

Fig. 22. (*continued*)

layer, the "∧" vortex stretches downstream with the interaction between the compression shock and vortex. In addition, the separation flow topology on the upper wall of the booster changes from the single node-saddle pattern to the node-saddle and double saddle-spirals pattern, as shown in Fig. 23 (f). As the orbiter further moves upstream, the leading-edge shock of the booster will no longer impinge on the orbiter lower wall and is about to interact with the wake of the orbiter, as illustrated in Fig. 22 (g). Moreover, the "∧" vortex is stretched and raised further so that the vortex surface separates from the upper wall of the booster, and there are no corresponding critical points and lines on the upper wall of the booster. When the orbiter is separated from the booster, the flow structure is dominated by compression shock/shock and shock/vortex interactions, as sketched in Fig. 22 (h). The orbiter is not disturbed by the booster, and the leading-edge shock of the orbiter interacts with the booster shock underneath the booster nose, resulting in the pressure on the lower wall of the booster rise and the nose-up moment of the booster increases. Additionally, the pitching angle and the moment of the orbiter are nearly zero, separated from the booster and in a completely controllable state.

In terms of the flowfields during LSS in the case of AoA = 10°, the flow structures before the orbiter separated from the booster are similar to those in the case of AoA = 5°. The notable difference in flow structure after the orbiter separates from the booster

is that the flowfield is dominated by SBLI occurring on the upper wall of the booster beside the shock/shock and shock/vortex interaction, as shown in Fig. 24. As AoA increases, the strength of the Leading-edge vortex is stronger than at AoA = 5°. Moreover, the leading-edge shock of the orbiter transmits the leading edge shock of the booster and impinges on the boundary layer of the upper wall of the booster, resulting in SBLI and recirculation zone on the booster. The predominant vortex on the booster, i.e., "∧" vortex, is displaced by the horseshoe vortex induced by SBLI. In addition, the limiting streamlines on the booster in Fig. 24 show that the separated topology on the booster is the typical saddle-node pattern, and the horseshoe vortex extends spanwise and interacts with the leading-edge vortex on the shoulder of the booster.

4.3. Comparison of interference load between the TSS and LSS schemes

After the independent discussion and analysis of characteristics for each stage separation scheme have been done, the advantages and disadvantages of the separation scheme should be addressed. Considering the safety of TSTO stage separation, the two stages should separate within a predetermined time without collision. Moreover, there is no strong interference between the two stages, and it is within the ability of the attitude control system so that the vehicle is prevented from the risk of instability and local surface deformation caused by the drastic loads. From the previous
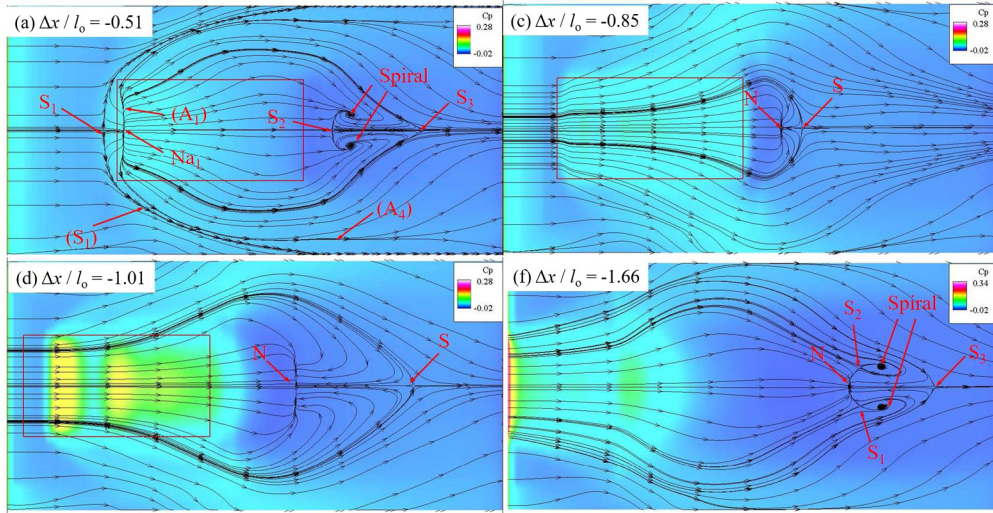
Fig. 23. Limiting streamlines (skin fraction lines) on the upper wall of the booster in the case of AoA = 5°.
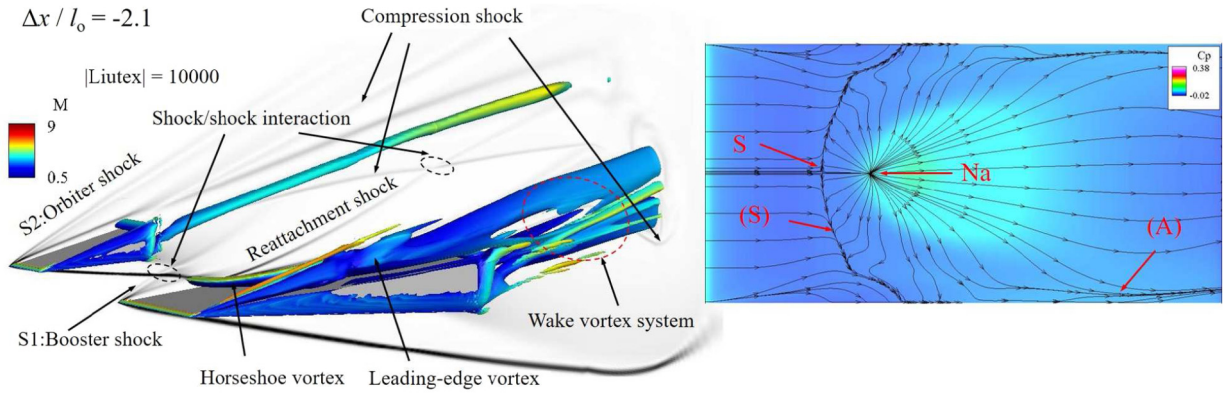

Fig. 24. Flow structure (left) and limiting streamlines on the upper wall of the booster (right) of $\Delta x/l_o = -2.1$ during LSS in the case of AoA = 10°.
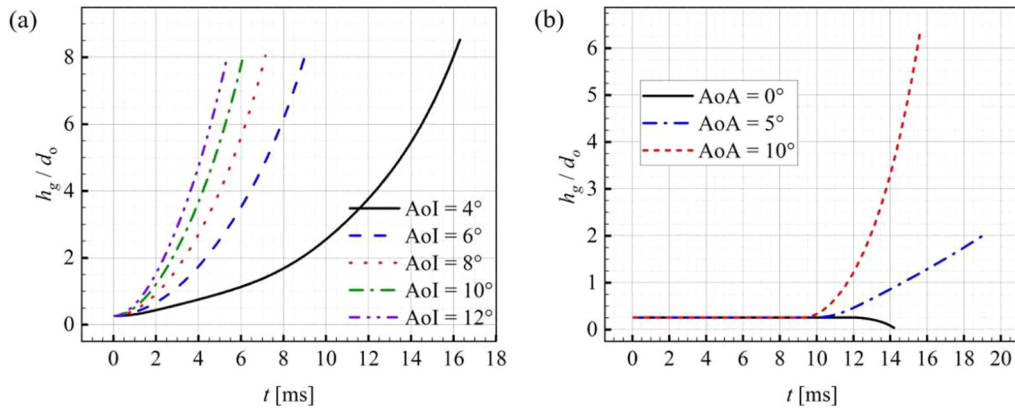

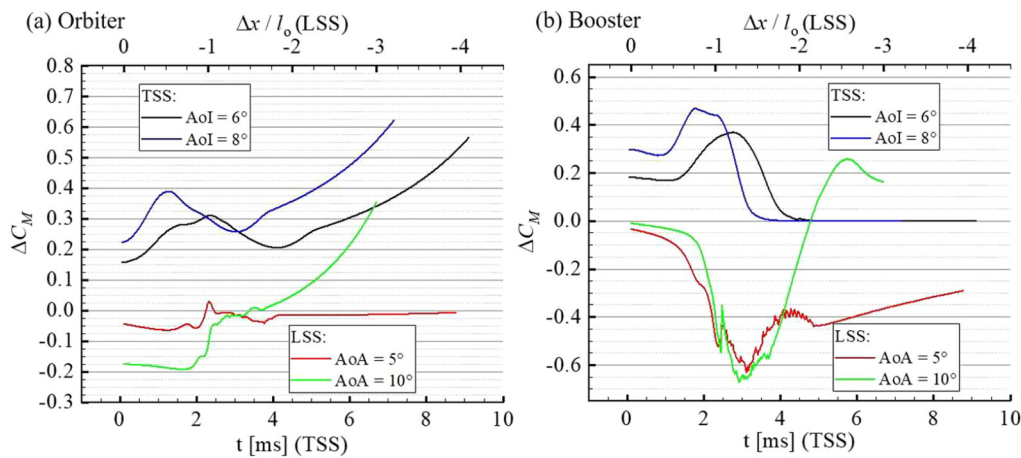**Fig. 25.** Minimum gap between two stages with time in TSS (a) and LSS (b) dynamic cases.

Fig. 26. Interference load (ΔC_M) of both stages during each separation scheme.

discussion, the proper condition of TSS is $6° <$ AoI $< 8°$ while the proper condition of LSS is the AoA slightly higher than $5°$. Fig. 25 presents the minimum gap (h_g) between stages as function of time in TSS and LSS dynamic cases, and Fig. 26 presents the interference load (ΔC_M) of both stages during each separation scheme. As shown in Fig. 25, for TSS dynamic cases, the orbiter is separated from booster faster and faster with the increasing of the AoI as the minimum gap increases steeper with increasing of the AoI. For LSS dynamic cases, the orbiter collides with the booster at AoA $= 0°$ as the minimum gap tends to zero around $t = 14$ ms while separates from the booster at AoA $= 5°$ and $10°$. Furthermore, the minimum gap between stages increases faster for TSS than that of for LSS, which means the orbiter will bear more normal overloads in TSS than that in LSS since stronger aerodynamic interference. As illustrated in Fig. 26, the interference load on the orbiter is smaller in LSS than that in TSS. Namely, the aerodynamic interferences, including SSI and SBLI, are weaker in LSS than those in TSS. This is a vital advantage because the orbiter is more important as a payload or manned vehicle for TSTO stage separation. Conversely, the interference load on the booster is slightly higher in LSS than that in TSS, which is dominated by the inherent character of LSS since the orbiter accelerates on the back of the booster and the aerodynamic interference moves forward with the orbiter. In this regard, both separation schemes are halved on a fifty-fifty basis. However, the LSS is favorable for the current TSTO model considering the interference load at both stages.

5. Conclusions

In the present study, hypersonic flow over a TSTO-like two-body system (i.e., a 3-D double wedge) is numerically simulated during transverse and longitudinal stage separation. For transverse stage separation (TSS), the flowfield is dominated by the strong shock wave/boundary layer interactions and horseshoe vortex system, and the intensity of the aerodynamic interference increases with increasing AoI, but decreases with the increase of clearance during stage separation. Moreover, the separation time gradually decreases with the increase of AoI, and the proper AoI conditions of TSS for the current TSTO model is $6°$ and $8°$. For longitudinal stage separation (LSS), the orbiter can safely separate from the booster at AoA $= 5°$ and $10°$ cases while the collision occurs at AoA $= 0°$ case. The proper AoA value of the safe LSS is $5°$. The flowfield of LSS is predominated by "∧" or horseshoe vortex system and a weak SBLI in clearance. Hence, aerodynamic interferences are weaker in LSS than that in TSS, and interference load on the orbiter is smaller in LSS than that in TSS. The LSS is favorable for TSTO separation, even if the time for the LSS maybe longer.

Declaration of competing interest

The authors declare that they have no known competing financial interests or personal relationships that could have appeared to influence the work reported in this paper.

Data availability

Data will be made available on request.

Acknowledgements

References

[1] W. Schroder, G. Hartmann, Analysis of inviscid and viscous hypersonic flows past a two-stage spacecraft, J. Spacecr. Rockets 30 (1993) 8–13.

[2] X. Xue, Y. Nakamura, K. Mori, C.-Y. Wen, H. Jia, Numerical investigation of effects of angle-of-attack on a parachute-like two-body system, Aerosp. Sci. Technol. 69 (2017) 370–386.

[3] W. Schroder, F. Mergler, Investigation of the Flowfield over Parallel-Arranged Launch Vehicles, AIAA 24th Fluid Dynamics Conference, American Institute of Aeronautics and Astronautics, Orlando, FL, 1993, AIAA 93-3060.

[4] J. Cheng, R. Chen, R. Qiu, W. Sun, Y. You, Aerothermodynamic study of two-stage-to-orbit system composed of wide-speed-range vehicle and rocket, Acta Astronaut. 183 (2020) 330–345.

[5] J. Jia, D. Fu, Z. He, Aerodynamic interactions of a reusable launch vehicle model with different nose configurations, Acta Astronaut. 177 (2020) 58–65.

[6] A. Viviani, A. Aprovitola, L. Iuspa, G. Pezzella, Aeroshape design of reusable re-entry vehicles by multidisciplinary optimization and computational fluid dynamics, Aerosp. Sci. Technol. 105 (2020) 106029.

[7] H. Zhou, X. Wang, N. Cui, Glide guidance for reusable launch vehicles using analytical dynamics, Aerosp. Sci. Technol. 98 (2020) 105678.

[8] J. Zhou, Y. Xiao, K. Liu, W. She, Preliminary analysis for a two-stage-to-orbit reusable launch vehicle, in: 20th AIAA International Space Planes and Hypersonic Systems and Technologies Conference, American Institute of Aeronautics and Astronautics, Glasgow, Scotland, 2015.

[9] P. Griesemer, J. Mueller, M. Paluszek, System design of a reusable, horizontal take-off/horizontal landing two stage to orbit vehicle, in: 46th AIAA/ASME/SAE/ASEE Joint Propulsion Conference & Exhibit, American Institute of Aeronautics and Astronautics, Nashville, TN, 2010.

[10] L. Yang, Z. Ye, W. Li, Q. Sun, Longitudinal aerodynamic modeling and verification for air-launch-to-orbit system during stage separation, Aerosp. Sci. Technol. 117 (2021) 106915.

[11] Y. Liu, Z. Qian, W. Lu, S. He, Numerical investigation on the safe stage-separation mode for a TSTO vehicle, Aerosp. Sci. Technol. 107 (2020) 106349.

[12] J.H. Jia, D.B. Fu, Z.P. He, J.F. Yang, L.J. Hu, Hypersonic aerodynamic interference investigation for a two-stage-to-orbit model, Acta Astronaut. 168 (2020) 138–145.

[13] A. Sarosh, D. Yun-Feng, The GA-ANN expert system for mass-model classification of TSTO surrogates, Aerosp. Sci. Technol. 48 (2016) 146–157.

[14] L. McKinney, D. Farrell, T. Bogar, J. Stemler, Investigation of TSTO propulsion system options, in: 14th AIAA/AHI Space Planes and Hypersonic Systems and Technologies Conference, American Institute of Aeronautics and Astronautics, Canberra, Australia, 2006.

[15] A.F. Dissel, A.P. Kothari, M.J. Lewis, Investigation of two-stage-to-orbit airbreathing launch-vehicle configurations, J. Spacecr. Rockets 43 (2006) 568–574.

[16] M.A. Moelyadi, C. Breitsamter, B. Laschka, Stage-separation aerodynamics of two-stage space transport systems Part 1: steady-state simulations, J. Spacecr. Rockets 45 (2008) 1230–1239.

[17] H. Ozawa, K. Hanai, K. Kitamura, K. Mori, Y. Nakamura, Experimental investigation of shear-layer/body interactions in TSTO at hypersonic speeds, in: 46th AIAA Aerospace Sciences Meeting and Exhibit, American Institute of Aeronautics and Astronautics, Reno, Nevada, 2008.

[18] H. Ozawa, K. Kitamura, K. Hanai, K. Mori, Y. Nakamura, Unsteady aerodynamic interaction between two bodies at hypersonic speed, Trans. Jpn. Soc. Aeronaut. Space Sci. 53 (2010) 114–121.

[19] K. Kitamura, I. Men'shov, Y. Nakamura, Shock/shock and shock/boundary-layer interactions in two-body configurations, in: 35th AIAA Fluid Dynamics Conference and Exhibit, American Institute of Aeronautics and Astronautics, Toronto, Ontario, Canada, 2005.

[20] K. Kitamura, T. Nakamura, I. Men'shov, Y. Nakamura, CFD analysis of aerodynamic interference between a delta wing and a hemisphere-cylinder, in: 42nd AIAA Aerospace Sciences Meeting and Exhibit, American Institute of Aeronautics and Astronautics, Reno, Nevada, 2004.

[21] W. Bordelon, A. Frost, D. Reed, Stage separation wind tunnel tests of a generic TSTO launch vehicle, in: 21st AIAA Applied Aerodynamics Conference, American Institute of Aeronautics and Astronautics, Orlando, Florida, 2003.

[22] P. Brenner, Numerical simulation of three-dimensional and unsteady aerodynamics about bodies in relative motion applied to a TSTO separation, in: 5th International Aerospace Planes and Hypersonics Technologies Conference, American Institute of Aeronautics and Astronautics, Munich, Germany, 1993.

[23] T. Cvrlje, C. Breitsamter, B. Laschka, Numerical simulation of the lateral aerodynamics of an orbital stage at stage separation flow conditions, Aerosp. Sci. Technol. 4 (2000) 157–171.

[24] A. Olejnik, A. Dziubiński, Ł. Kiszkowiak, Separation safety analysis using CFD simulation and remeshing, Aerosp. Sci. Technol. (2020) 106190.

[25] W. Song, B. Ai, X. Zhao, Prediction and evaluation of the stage-separation compatibility of an internally carried air-launch vehicle, Aerosp. Sci. Technol. 105 (2020) 106001.

[26] F. Xue, Y.C. Wang, H. Qin, Derivation and validation of wind tunnel free-flight similarity law for store separation from aircraft, Aerosp. Sci. Technol. 97 (2020) 9.

[27] Y. Wang, H. Ozawa, H. Koyama, Y. Nakamura, Abort separation of launch escape system using aerodynamic interference, AIAA J. 51 (2012) 270–275.

[28] Y.P. Wang, H. Ozawa, Y. Nakamura, Numerical investigation of supersonic oscillatory flow with strong interference over a capsule-shaped abort system, Trans. Jpn. Soc. Aeronaut. Space Sci. 55 (2012) 286–294.

[29] Y. Wang, Y. Nakamura, Supersonic unsteady flow around a capsule-shaped abort system with angle of attack, Int. J. Aerosp. Lightw. Str. (IJALS) 1 (2011) 133–142.

[30] S. Weingertner, SAENGER - the reference concept of the German hypersonics technology program, in: 5th International Aerospace Planes and Hypersonics Technologies Conference, American Institute of Aeronautics and Astronautics, Munich, Germany, 1993.

[31] Z. Liu, X. Wang, G. Wang, Space Separation Design, China Astronautic Publishing House, Beijing, 2017, pp. 5–6.

[32] H. Luo, J. Baum, R. Lohner, Extension of HLLC scheme for flows at all speeds, in: 16th AIAA Computational Fluid Dynamics Conference, American Institute of Aeronautics and Astronautics, Orlando, Florida, 2003.

[33] E.F. Toro, Flux limiter methods, in: E.F. Toro (Ed.), Riemann Solvers and Numerical Methods for Fluid Dynamics, a Practical Introduction, 3 edn., Springer, New York, 2009, pp. 456–485.

[34] W. Sutherland, The viscosity of gases and molecular force, Philosophical (1893) 507–531.

[35] J.R. Edwards, An implicit multigrid algorithm for computing hypersonic, chemically reacting viscous flows, J. Comput. Phys. 123 (1996) 84–95.

[36] X. Xue, Y. Nishiyama, Y. Nakamura, K. Mori, Y. Wang, C. Wen, High-speed unsteady flows past two-body configurations, Chin. J. Aeronaut. 31 (2018) 54–64.

[37] K. Kitamura, A. Nishino, T. Ishikawa, I. Men'shov, Y. Nakamura, A device for reduction of heat flux produced by hypersonic shock interference, in: 34th AIAA Fluid Dynamics Conference and Exhibit, American Institute of Aeronautics and Astronautics, Portland, Oregon, 2004.

[38] K. Hanai, H. Ozawa, Y. Nakamura, Two-stage-to-orbit booster configuration for reducing aerodynamic heating at hypersonic speed, in: 37th AIAA Fluid Dynamics Conference and Exhibit, American Institute of Aeronautics and Astronautics, Miami, FL, 2007.

[39] S. Tian, J. Fu, J. Chen, A numerical method for multi-body separation with collisions, Aerosp. Sci. Technol. 109 (2021) 106426.

[40] Z. Liu, X. Wang, G. Wang, Space Separation Design, China Astronautic Publishing House, Beijing, 2017, pp. 11–17.

[41] Y. Gao, C. Liu, Rortex and comparison with eigenvalue-based vortex identification criteria, Phys. Fluids 30 (2018) 085107.

[42] C. Liu, Y. Gao, S. Tian, X. Dong, Rortex—a new vortex vector definition and vorticity tensor and vector decompositions, Phys. Fluids 30 (2018) 035103.

[43] Y. Wang, Y. Gao, C. Liu, Letter: Galilean invariance of Rortex, Phys. Fluids 30 (2018) 111701.

[44] C. Liu, Y.-s. Gao, X.-r. Dong, Y.-q. Wang, J.-m. Liu, Y.-n. Zhang, X.-s. Cai, N. Gui, Third generation of vortex identification methods: omega and Liutex/Rortex based systems, J. Hydrodyn. 31 (2019) 205–223.

[45] S. Zaghi, A. Di Mascio, R. Broglia, R. Muscari, Application of dynamic overlapping grids to the simulation of the flow around a fully-appended submarine, Math. Comput. Simul. 116 (2015) 75–88.

[46] G. Degrez, C.H. Boccadoro, J.F. Wendt, The interaction of an oblique shock wave with a laminar boundary layer revisited. An experimental and numerical study, J. Fluid Mech. 177 (1987) 247–263.

[47] R.R. Heim, CFD wing/pylon/finned store mutual interference wind tunnel experiment, 1991, AEDC-TSR-91-P4.

[48] D. Snyder, E. Koutsavdis, J. Anttonen, Transonic Store Separation Using Unstructured CFD with Dynamic Meshing, 33rd AIAA Fluid Dynamics Conference and Exhibit, American Institute of Aeronautics and Astronautics, Orlando, Florida, 2003.